













Magneto-acoustic protein nanostructures for non-invasive imaging of tissue mechanics in vivo

Received: 26 May 2022

Accepted: 12 September 2023

Published online: 16 October 2023

 Check for updates

Whee-Soo Kim ^{1,2,3,11}, Sungjin Min ^{4,11}, Su Kyeom Kim⁴, Sunghwi Kang^{1,3,5}, Soohwan An ⁴, Ernesto Criado-Hidalgo ², Hunter Davis², Avinoam Bar-Zion², Dina Malounda², Yu Heun Kim⁴, Jae-Hyun Lee ^{1,3}, Soo Han Bae^{6,7}, Jin Gu Lee⁸, Minsuk Kwak ^{1,3}, Seung-Woo Cho ^{1,3,4} , Mikhail G. Shapiro ^{1,2,3,9,10}  & Jinwoo Cheon ^{1,3,5} 

Measuring cellular and tissue mechanics inside intact living organisms is essential for interrogating the roles of force in physiological and disease processes. Current agents for studying the mechanobiology of intact, living organisms are limited by poor light penetration and material stability. Magnetomotive ultrasound is an emerging modality for real-time in vivo imaging of tissue mechanics. Nonetheless, it has poor sensitivity and spatiotemporal resolution. Here we describe magneto-gas vesicles (MGVs), protein nanostructures based on gas vesicles and magnetic nanoparticles that produce differential ultrasound signals in response to varying mechanical properties of surrounding tissues. These hybrid nanomaterials significantly improve signal strength and detection sensitivity. Furthermore, MGVs enable non-invasive, long-term and quantitative measurements of mechanical properties within three-dimensional tissues and in vivo fibrosis models. Using MGVs as novel contrast agents, we demonstrate their potential for non-invasive imaging of tissue elasticity, offering insights into mechanobiology and its application to disease diagnosis and treatment.

Tissue mechanical properties play a crucial role in various cellular processes, including morphogenesis, tissue homeostasis and disease progression¹. Among these properties, tissue stiffness is notably altered in numerous pathological conditions such as cancer, diabetes, cardiovascular disease and fibrosis¹. However, accurately measuring

localized tissue stiffness within deep, living three-dimensional (3D) tissues remains challenging². Existing techniques primarily focus on subcellular measurements, are limited to in vitro cultures or dissected tissues and are unable to capture local variations in tissue stiffness^{3–8}. Ultrasound-based shear-wave elastography offers non-invasive and

¹Center for Nanomedicine, Institute for Basic Science (IBS), Seoul, Republic of Korea. ²Division of Chemistry and Chemical Engineering, California Institute of Technology, Pasadena, CA, USA. ³Department of Nano Biomedical Engineering (NanoBME), Advanced Science Institute, Yonsei University, Seoul, Republic of Korea. ⁴Department of Biotechnology, Yonsei University, Seoul, Republic of Korea. ⁵Department of Chemistry, Yonsei University, Seoul, Republic of Korea. ⁶Severance Biomedical Science Institute, Yonsei Biomedical Research Institute, Yonsei University College of Medicine, Seoul, Republic of Korea. ⁷Severance Biomedical Science Institute, Graduate School of Medical Science, Brain Korea 21 Project, Yonsei University College of Medicine, Seoul, Republic of Korea. ⁸Department of Thoracic and Cardiovascular Surgery, Severance Hospital, Yonsei University College of Medicine, Seoul, Republic of Korea. ⁹Andrew and Peggy Cherng Department of Medical Engineering, California Institute of Technology, Pasadena, CA, USA. ¹⁰Howard Hughes Medical Institute, Pasadena, CA, USA. ¹¹These authors contributed equally: Whee-Soo Kim, Sungjin Min. ✉ e-mail: seungwoocho@yonsei.ac.kr; mikhail@caltech.edu; jcheon@yonsei.ac.kr

quantitative assessment of in vivo tissue stiffness, but its resolution may be limited in detecting small tumours, resolving boundaries between tumours and surrounding tissue and assessing wave speed fluctuation in different tissue types⁹. Recent advances in injectable and deformable materials have enabled the measurement of local mechanical properties in intact soft tissues, but these methods often rely on fluorescent probes and optical imaging, making deployment in deep tissues challenging and limiting long-term measurements due to sensitivity to local factors such as pH and temperature^{10–13}. Thus, improved methodologies to accurately measure tissue mechanics in vivo are required.

Magnetomotive ultrasound imaging (MMUS) has emerged as a potential method for measuring tissue mechanics in vivo, but faces challenges due to suboptimal contrast agents resulting in limited resolution and poor sensitivity^{14–16}. To address these limitations, we combined gas vesicles (GVs)—air-filled protein nanostructures with highly sensitive ultrasound contrast^{17–19}—with superparamagnetic nanoparticles (MNPs) to develop a new class of hybrid protein nanostructures called magneto-GVs (MGVs). Chemical linking of MNPs to GV proteins significantly improves signal strength and sensitivity compared with conventional MMUS contrast agents. We hypothesize that as the mobility of MNPs is affected by the surrounding mechanical properties, MGVs dynamically alter MMUS contrast in response to tissue mechanics, enabling non-invasive and quantitative measurement of tissue stiffness in vivo. We demonstrate that MGVs have the potential for long-term disease monitoring and drug screening in 3D organoid and in vivo fibrosis models due to their excellent stability, enabling robust and reproducible imaging.

Synthesis of MGVs with improved imaging contrast

To determine whether the combination of particles with high acoustic contrast and strong superparamagnetism can improve MMUS imaging capability, we synthesized magnetic nanoparticle-conjugated gas vesicles (MGVs). We established the MMUS imaging system and optimized the system's magnetic properties using standard magnetic microparticles (Fig. 1a and Supplementary Fig. 1). Based on the MMUS signal intensity, magnetic parameters of 5 Hz, 30 mT and sine wave were chosen as the frequency, maximum field strength and temporal pattern of the electromagnetic field, respectively (Supplementary Fig. 1a–c). Zinc-doped iron oxide MNPs were synthesized and functionalized with azide groups, as previously reported²⁰. We purified GV proteins from the cyanobacterium *Anabaena flos-aquae*²¹, and added dibenzocyclooctyne (DBCO) to the GV protein surface through an NH₂–NHS reaction. MGVs were finally synthesized by conjugating azide-functionalized MNPs and DBCO-GVs via click chemistry (Fig. 1b). After a 4 h conjugation reaction, MGVs could be isolated from a suspension of unbound MNPs using buoyancy purification (Fig. 1d). MGVs had a hydrodynamic diameter of approximately 494.1 ± 11.5 nm, while functionalized GV proteins had a diameter of approximately 272 ± 4.5 nm (Fig. 1e). MGVs were stable in different media conditions or during prolonged storage (Supplementary Fig. 2a,b). The conjugation ratio of MNPs to GV proteins was approximately 186 MNPs per GV (Fig. 1c and Supplementary Fig. 3). The

magnetic moment of MGVs was 79 emu g⁻¹, which was comparable to that of MNPs (Fig. 1f).

We next assessed the ability of MGV protein nanostructures to produce robust MMUS signals in response to applied magnetic fields. Using the optimized magnetic conditions identified above, we performed a head-to-head comparison of GV proteins, MNPs and MGVs with MMUS imaging in agarose phantoms. The concentrations of all materials were matched based on inductively coupled plasma mass spectrometry (ICPMS) measurements and B-mode imaging (Fig. 1g and Supplementary Fig. 3). MGVs showed superior sensitivity and spatiotemporal control compared with other nanomaterials, while MMUS imaging retained the spatial resolution of conventional B-mode ultrasound (Supplementary Fig. 4). Furthermore, despite differences in hydrodynamic size possibly attributed to MNP conjugation, GV proteins and MGVs showed similar acoustic responses, suggesting the differences in MMUS signals are not due to distinct sound-scattering properties (Supplementary Fig. 5). Magnetic stimulation of MGVs resulted in robust time-locked ultrasound signals, which ceased when the magnetic field was removed (Fig. 1g). The signal-to-background ratio (SBR) of the average pixel intensity was used to quantify MMUS signals. MGVs achieved a 12-fold higher magnetic-field-dependent signal intensity change (Δ , SBR = 110.1 ± 21.3) than GV proteins (9.1 ± 8.7) (Fig. 1g–j). In addition, MGVs produced a significant increase in signal compared to MNPs (25.6 ± 16.6) or MNPs with tissue-mimicking materials (Al₂O₃) (26.5 ± 14.9), suggesting the ability of GV proteins conjugated to MNPs to transduce magnetic stimulation and produce ultrasound contrast for improved MMUS sensitivity (Fig. 1g–j).

To evaluate the performance limits of MGV-based MMUS imaging, we imaged dispersions containing MGVs, GV proteins and MNPs at a fixed concentration of 0.4 nM in 0.1% agarose while applying magnetic fields of increasing strength (7–30 mT). MGVs exhibited a robust magnetic MMUS response, with detectable signals from 10 mT to 30 mT. In contrast, GV proteins showed no visible contrast, while MNPs produced weaker signals only at ≥30 mT (Fig. 1h–k). To assess the sensitivity of the MGV-based approach relative to other nanomaterials, we performed MMUS imaging of a concentration series of MGVs, GV proteins and MNPs in agarose phantoms with a constant 30 mT magnetic field. MGVs produced significantly higher MMUS signals than the other control materials when the concentration was in the range of 0.05–0.4 nM (Fig. 1i–l). MGVs attained an excellent SBR with a limit of detection of 0.05 nM, representing >8-fold enhancement in sensitivity relative to conventional MNP-based MMUS imaging (Fig. 1i–l). Comparing our results to previous MNP-based MMUS imaging, MGVs showed unique sensitivity to low MNP concentrations and weak magnetic fields (Supplementary Fig. 6). Altogether, these results validate MGVs as novel contrast agents for MMUS imaging with enhanced ultrasound contrast and detection sensitivity.

Dynamic range of stiffness measurement with MGVs

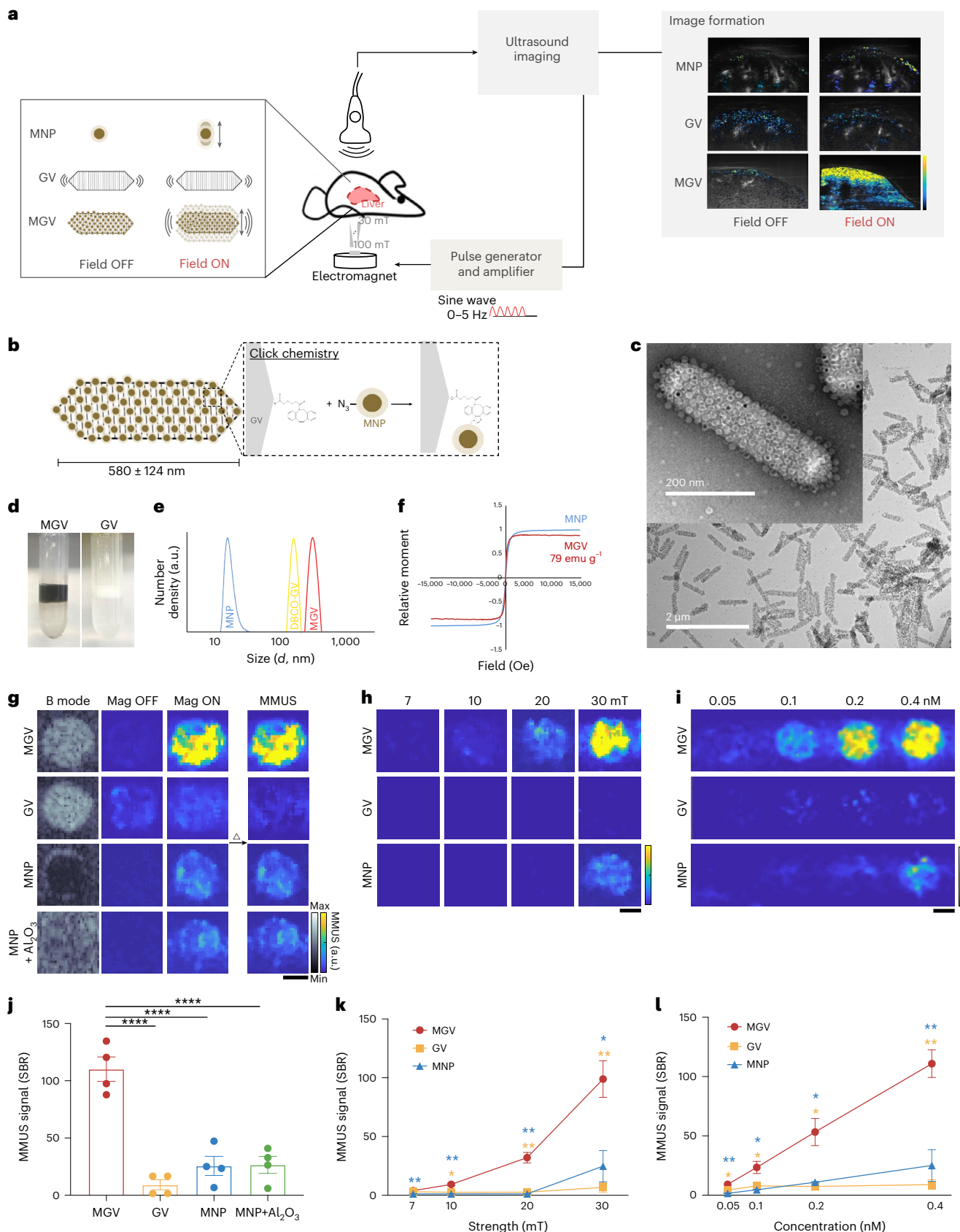
The material stiffness influences the magnetically induced motion of MNPs¹⁵. Whereas softer materials would allow more MGV movement

Fig. 1 | Development and characterization of the MMUS imaging system and MGVs. **a**, Schematic illustration showing the set-up and working principle of the MGV-based MMUS imaging system. **b**, Schematic illustration of conjugating MNPs to GV proteins using click chemistry to form MGVs. **c**, TEM image of fabricated MGVs. **d**, Images of MGVs and GV proteins after buoyancy purification. **e**, The hydrodynamic size of MGVs, MNPs and GV proteins with functionalized DBCO by dynamic light scattering. **f**, The magnetic moment of MGVs and MNPs measured by a vibrating-sample magnetometer. **g**, Comparison of MMUS imaging between MGVs, GV proteins and MNPs in 0.1% (w/v) agarose phantom using 0.4 nM MGVs, where 0.4 nM MGVs represent 456 pM of GV proteins and 76 nM of MNPs. $n = 4$ independent experiments. **h**, Magnetic strength-dependent MMUS images obtained from 7 mT to 30 mT using 0.4 nM MGVs. $n = 3$ independent experiments. **i**, Concentration-dependent MMUS images

of different groups. $n = 3$ independent experiments. **j–l**, SBR quantification of MMUS images from different cohorts (P (left–right) = 0.00006564, 0.000040719, 0.000045239) (**j**), with varying magnetic strength (P (blue, left–right) = 0.005394, 0.002267, 0.002239, 0.022173; P (yellow, left–right) = 0.590133, 0.012733, 0.003060, 0.004556) (**k**) and concentration (P (blue, left–right) = 0.004505, 0.020735, 0.021156, 0.008343; P (yellow, left–right) = 0.029392, 0.044301, 0.018321, 0.001178) (**l**) for the same conditions as in **g–i**. Scale bars in **g–i**, 1 mm. Min and max on the parula (MMUS) and grey (B-mode) colour bars represent 0 and 10,000 arbitrary units, respectively. In **j–l** lines and error bars represent mean ± s.e.m., and significance was determined using one-way analysis of variance (ANOVA) with Tukey's multiple-comparisons test (**j**) and a multiple unpaired two-sided t -test (**k, l**): * $P < 0.05$, ** $P < 0.01$, *** $P < 0.001$, **** $P < 0.0001$.

and induce stronger ultrasound scattering, stiffer materials would restrict MGVS motion in response to applied magnetic fields, leading to a decrease in MMUS signal (Fig. 2a). To test the ability of MGVS to quantitatively measure the stiffness of surrounding materials, we performed

MMUS imaging in vitro of MGVS embedded in agarose phantoms with varying elastic modulus, ranging from 74 Pa to 5,828 Pa (Fig. 2b). As predicted, we observed an inverse relationship of MGVS signals as a function of increasing elastic modulus of the agarose phantoms. At fixed MGVS



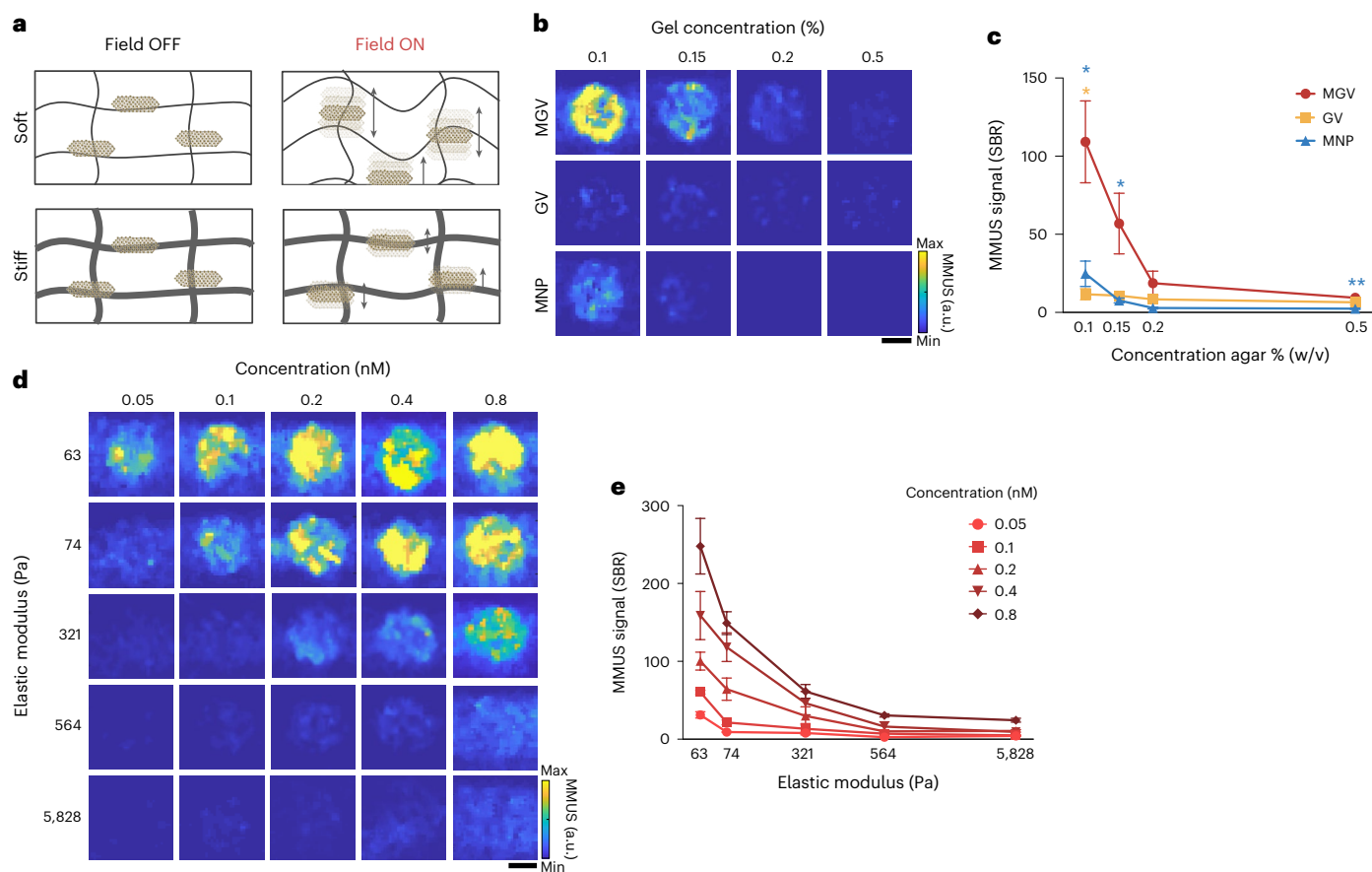


Fig. 2 | Stiffness-dependent MMUS imaging. **a**, Schematic illustration showing the movement of MGVs inside soft and stiff materials when an applied magnetic field is off and on. **b, c**, MMUS images (**b**) and SBR quantification (**c**) of agarose-concentration-dependent movement of MGVs ranging from 0.1% to 0.5% (w/v) agarose. P (blue, left–right) = 0.021665, 0.044665, 0.082836, 0.004661; P (yellow, left–right) = 0.010210, 0.054968, 0.228487, 0.231079. $n = 4$ independent experiments. **d, e**, MMUS images (**d**) and SBR quantification

(**e**) based on different values of elastic modulus and concentration. $n = 5$ independent experiments. Scale bars, 1 mm. Min and max on the colour bars represent 0 and 10,000 arbitrary units, respectively. Lines and error bars represent mean \pm s.e.m., and significance was determined using a multiple unpaired two-sided t -test (**c**) and one-way ANOVA with Tukey's multiple-comparisons test (**e**): * $P < 0.05$, ** $P < 0.01$, *** $P < 0.001$, **** $P < 0.0001$.

concentrations ($OD_{500} = 4$, 0.4 nM) and magnetic field (30 mT), MGVs in 0.1% agarose ($SBR = 109.1 \pm 52.3$) produced a 2- and 6-fold greater MMUS signal intensity change than in 0.15% agarose (56.9 ± 38.8) and 0.2% agarose (18.7 ± 15.3), respectively, while generating negligible signal in 0.5% agarose phantom (9.3 ± 3.1) (Fig. 2b,c). Although the MNP-only sample showed stiffness-dependent signal intensity changes, its MMUS signal was significantly weaker than that of MGVs, leading to lower detection sensitivity of material stiffness (Fig. 2b,c). These results together demonstrate that MGVs embedded in phantoms with lower elastic moduli experience more strain from the same applied magnetic gradient force, resulting in larger vibration amplitudes and stronger ultrasound signals.

To determine whether MGVs can more precisely quantify a wide range of material stiffness values, we used two in vitro phantoms created from two different hydrogel systems with varying stiffness (Fig. 2d and Supplementary Fig. 7). Matrigel-based phantoms were used for softer materials (63 Pa), and agarose gel phantoms were used for materials with elastic moduli ranging from 74 to 5,828 Pa. We observed that the detection range varies with MGV concentration (Fig. 2d,e). The MMUS signal was clearly differentiated in a range of around 63 Pa ($SBR = 100.2 \pm 31.7$) to 564 Pa (10.0 ± 6.9) when using 0.2 nM MGVs, whereas the detection range broadened to 5,828 Pa (24.3 ± 4.9) when using 0.8 nM MGVs (Fig. 2d,e). Furthermore, when very small amounts of MGVs (0.05 nM) were used, the MMUS signal was only visible until

74 Pa, indicating that at this concentration, MGVs are capable of detecting stiffness changes in materials with elastic moduli of less than 74 Pa (Fig. 2d,e). These findings show that depending on the tissue being measured, MGV concentration can be adjusted to generate enhanced or attenuated signals for the acquisition of more accurate MMUS images in diverse tissue types.

In addition, we imaged MGVs in polyacrylamide gels of various stiffnesses and similar pore sizes (Supplementary Table 1)^{12,22,23}, and found an inverse relationship between MMUS signals and stiffness (Extended Data Fig. 1a,b). Furthermore, signal attenuation differences between materials of different stiffnesses were much smaller than the differences in MMUS signals (Supplementary Fig. 8). These results indicate that MMUS imaging can measure stiffness regardless of material composition and pore size (Supplementary Note 1). In vitro cytotoxicity assays showed that treatment with MGVs did not have any significant impact on cellular viability (Supplementary Fig. 9a).

MGV ability as a stiffness sensor for lung organoid fibrosis

Organoids are miniature organ-like constructs and represent a novel in vitro platform for studying disease development²⁴. We developed a lung organoid fibrosis model to assess the potential of MGVs for monitoring 3D microenvironment stiffness, aiming to diagnose and observe lung fibrosis progression. Fibrosis was induced in lung organoids using

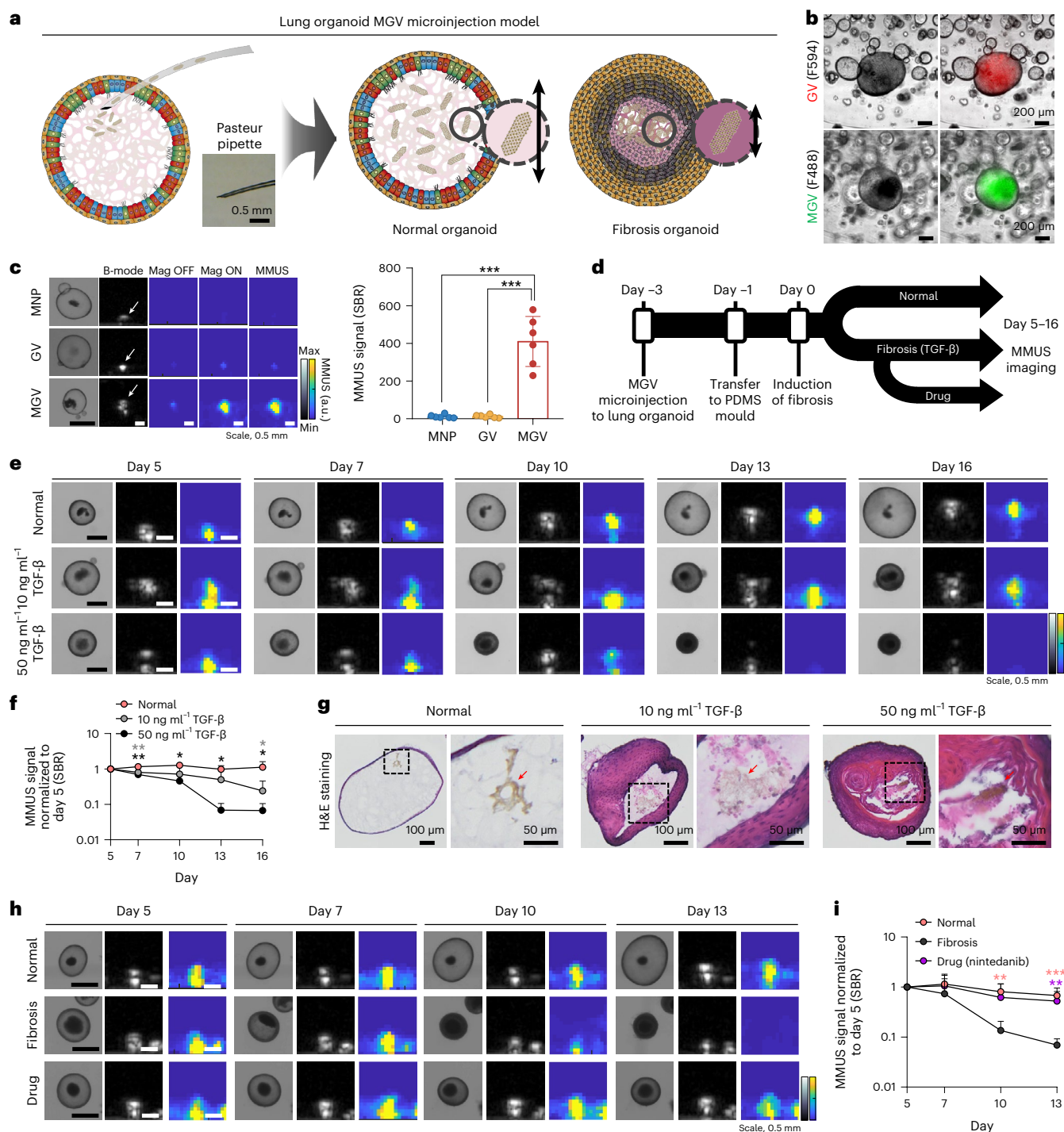


Fig. 3 | MGVB-based MMUS imaging for monitoring fibrosis in a human lung organoid model. **a**, Schematic illustration showing microinjection of MGVBs into a lung organoid and detection of stiffness change. **b**, Bright-field and merged fluorescence images of GVs and MGVBs in lung organoids. $n = 2$ biological replicates examined in one experiment. **c**, Bright-field, B-mode and MMUS images and quantification of microinjected lung organoids with MNPs, GVs and MGVBs. P (left–right) = 0.00000061, 0.00000062. $n = 6$ biological replicates examined in one experiment. **d**, Experimental timeline of the preparation of MGVB-microinjected lung organoid models and MMUS imaging. **e, f**, Bright-field, B-mode, MMUS images (**e**) and SBR quantification (**f**) of MGVB-microinjected lung organoids (normal and two fibrosis models). Images were taken from day 5 to day 16 after fibrosis induction. Quantification was conducted using relative MMUS SBR signal normalized to the day 5 value in normal and fibrosis groups. For day 7–16, P (grey, left–right) = 0.008486, 0.136217, 0.240127, 0.028171; P (black, left–right) = 0.002438, 0.036369, 0.032499, 0.012792. $n = 3$ biological replicates

examined in two experiments. **g**, H&E staining of organoid sections in normal and fibrosis groups. Red arrows indicate the localization of MGVBs in the organoids. $n = 1$ biological replicate examined in two experiments.

h, i, Bright-field, B-mode, MMUS images (**h**) and SBR quantification (**i**) of MGVB-microinjected lung organoids in the normal group, fibrosis group (50 ng ml^{-1} TGF- β) and drug-treated fibrosis group (50 ng ml^{-1} TGF- β + $10 \mu\text{M}$ nintedanib). Images were taken from day 5 to day 13 after fibrosis induction. Quantification was conducted using relative MMUS SBR signal normalized to the day 5 value in different organoid groups. For day 7–13, P (salmon, left–right) = 0.518531, 0.009231, 0.000368; P (purple, left–right) = 0.667557, 0.063610, 0.005257. $n = 7$ biological replicates examined in one experiment. Min and max on the parula (MMUS) and grey (B-mode) colour bars represent 0 and 20,000 arbitrary units. All lines and error bars represent mean \pm s.d., and significance was determined using one-way ANOVA with Tukey’s multiple-comparisons test in **c, f, i**: * $P < 0.05$, ** $P < 0.01$, *** $P < 0.001$.

transforming growth factor- β (TGF- β)^{25–27}, resulting in decreased organoid size corresponding to fibrosis severity (Extended Data Fig. 2).

To demonstrate the capability of MGV-based MMUS imaging for sensitive detection of fibrosis progression in a lung organoid model, MGVs were microinjected into the lumen of lung organoids, and the difference in MMUS signals was compared between normal and fibrosis organoids (Fig. 3a). Microinjection of MGVs conjugated with fluorescence markers showed that MGVs filled the lumen of lung organoids and remained there for 19 days without leakage (Fig. 3b and Extended Data Fig. 3). Consistent with *in vitro* experiments, MGVs (SBR = 410.1 ± 132.8) produced 32- and 33-fold enhanced MMUS signals compared with GVs (12.7 ± 8.2) and MNPs (12.1 ± 9.3) in the lumen of lung organoids (Fig. 3c). We hypothesized that fibrotic organoids would exhibit an increased stiffness, which would suppress the magnetically induced movements of MGVs and thus result in weaker MMUS signals (Fig. 3d). Organoids were moved to a polydimethylsiloxane (PDMS) mould 2 days after microinjection, and the next day fibrosis in MGV-injected organoids was induced with TGF- β treatment. MMUS imaging was performed from day 5 to 16 after the induction of fibrosis. The intensity of MMUS signals gradually decreased in the fibrotic lung organoids over a culture period and the decrease in signal was more evident in the organoids treated with 50 ng ml^{-1} TGF- β (Fig. 3e,f). Our results demonstrate that MMUS imaging using MGVs could provide substantial advantages in the detection of fibrosis over other techniques by allowing real-time monitoring of stiffness changes in live lung organoids without fixation.

Then, the increased fibrosis-induced stiffness in organoids observed by MMUS was validated. Haematoxylin & eosin (H&E) staining revealed thickening of the epithelium layer, abnormal cell growth and MGV localization in the lumen of TGF- β -treated lung organoids in a dose-dependent manner (Fig. 3g). Moreover, in fibrotic lung organoids treated with TGF- β , markers of ciliated (α -tubulin) and goblet (MUC5AC) cells were reduced, while P63-positive basal cells and markers of the epithelial-to-mesenchymal transition (smooth muscle actin (SMA) and vimentin (VIM)) were increased (Extended Data Fig. 4), similar to observations in patients with idiopathic pulmonary fibrosis²⁸. Finally, we examined the feasibility of the MGV-bearing lung organoid model for evaluating the efficacy of antifibrosis drugs (Fig. 3h). Nintedanib, well known for its antifibrotic effects on idiopathic pulmonary fibrosis, was tested, and treatment was performed starting from day 5 after fibrosis induction²⁹. MMUS signals decreased in organoids with TGF- β -induced fibrosis, but the signals in lung fibrosis organoids treated with drug were maintained at a similar level to that of normal organoids (Fig. 3h,i). MGV imaging in a lung organoid could be used to screen therapeutic drugs for lung fibrosis.

MGV-based MMUS imaging in a liver organoid fibrosis model

The liver is another important organ for fibrosis modelling, and stiffness is known as an important indicator of the fibrotic liver disease³⁰. Accordingly, we tested MGV-based MMUS imaging for detecting the increase in stiffness in a liver fibrosis organoid model. Four types of cells (hepatic endodermal cells, hepatic stellate cells, endothelial cells and mesenchymal cells) were encapsulated in collagen hydrogel containing MGVs, resulting in generation of MGV-incorporated liver organoids (Fig. 4a). This technique allowed localization of MGVs in the extracellular matrix (ECM) in organoids, where the increase in stiffness occurs³¹. Because hepatic stellate cells play an important role in liver fibrosis and collagen is an ECM component highly correlated with increased stiffness in liver fibrosis, our platform contains both cellular and extracellular components suitable for fibrosis modelling. The co-localization of hepatic endodermal cells and hepatic stellate cells in the MGV-incorporated liver organoids suggests that our organoids create a physiologically accurate liver model (Fig. 4b).

Induction of fibrosis in liver organoids was done in the same manner as in the lung organoids, and MMUS imaging was performed from

0 to 7 days after induction (Fig. 4c). Although normal and fibrosis liver organoids did not show morphological differences, there was a significant difference in the intensity of the MMUS signals over the culture period (Fig. 4d,e). Interestingly, the MMUS signal intensity increased gradually during the culture of normal liver organoids, indicating a natural decrease in organoid stiffness over time due to active ECM remodelling^{32–34}. In normal tissue, ECM homeostasis is regulated by repeated cycles of ECM degradation and synthesis^{32,35}. Histological analyses show that the continuous collagen degradation by MMP2 enzymes contributes to the decreased stiffness and increased MMUS intensity of the liver organoids during the culture (Extended Data Fig. 5a–c)³⁶. The presence of MGVs in each organoid model was affirmed through H&E staining (Fig. 4f). The upregulation of a fibrotic marker (VIM) and the reduction of a mature hepatic marker (albumin (ALB)) confirmed the induction of fibrosis in liver organoids treated with TGF- β (Fig. 4g). Finally, we examined the applicability of MGV-incorporated liver organoid models to test drugs to treat liver fibrosis. The intensity of MMUS signals in fibrotic liver organoids treated with obeticholic acid (SBR = 9.6 ± 1.2), a drug known to prevent or retard liver fibrosis, was significantly higher than that of the fibrotic organoids without drug treatment (3.5 ± 0.3) (Fig. 4h,i), indicating a notable reduction in stiffness and alleviation of fibrosis by treatment with obeticholic acid. These data demonstrate the possibility of using MGV-incorporated liver organoids as a drug-screening platform for liver fibrosis. The combination of MGV-based MMUS imaging and organoid could also be utilized for other diseases in which a change in stiffness is an important diagnostic indicator, such as acidosis of the brain and cancers^{32,33}.

MGV signal detection in animal liver tissues

Having demonstrated the ability of MGVs to serve as both MMUS contrast agents and a stiffness sensor *in vitro* and *in cellulo*, we tested their capabilities in *ex vivo* and *in vivo* animal tissues. To compare their performance as MMUS contrast agents, we performed intravenous injections of MGVs, GVs and MNPs in live mice. To facilitate more specific GV imaging against tissue background, Ana GVs were modified to enhance nonlinear ultrasound contrast under amplitude modulation (AM)³⁷. At 5 min post-injection, the liver was removed for *ex vivo* MMUS imaging (Fig. 5a). The liver was chosen as our model organ because imaging stiffness would be useful for detecting diseases in this organ. In addition, GVs naturally accumulate throughout the liver upon intravenous administration^{38,39}. We expected intravenously administered MGVs to be rapidly taken up by the liver, resulting in strong ultrasound contrast in the organ. MGVs were evenly distributed in liver tissue after injection (Supplementary Fig. 10). We observed clear, robust MMUS contrast by MGVs, which exhibited 10-fold stronger signals than those produced by GVs and MNPs (Fig. 5b,c). To demonstrate that MGVs are capable of measuring the mechanical properties of tissues *ex vivo*, MMUS imaging was done in liver samples fixed with 10% formalin for 48 h⁴⁰. After formalin fixation, the MMUS signals from injected MGVs significantly decreased, corresponding to an increase in tissue stiffness (Fig. 5b,c). The difference in signal attenuation between normal and fixed livers was smaller than that of MMUS signals, indicating that signal differences in MMUS are not primarily influenced by attenuation intrinsic to the tissue (Supplementary Fig. 8). Meanwhile, non-magnetomotive AM ultrasound images showed consistent ultrasound contrast from MGVs before and after fixation, indicating the changes in MMUS signals in the fixed liver are not caused by the collapse or removal of MGVs, but rather by the restricted movement of MGVs (Extended Data Fig. 6). Thus, *ex vivo* liver imaging demonstrated that increasing stiffness lowered the MMUS signal, similarly as in the organoid model.

In vivo MMUS imaging of live animals is challenging due to skin reflection and breathing artefacts. B-mode and Doppler imaging were used to locate the liver, while ultrafast amplitude modulation (uAM) imaging could visualize robust contrast from MGVs and GVs in the liver (Fig. 5e and Extended Data Fig. 7). After confirming their localization,

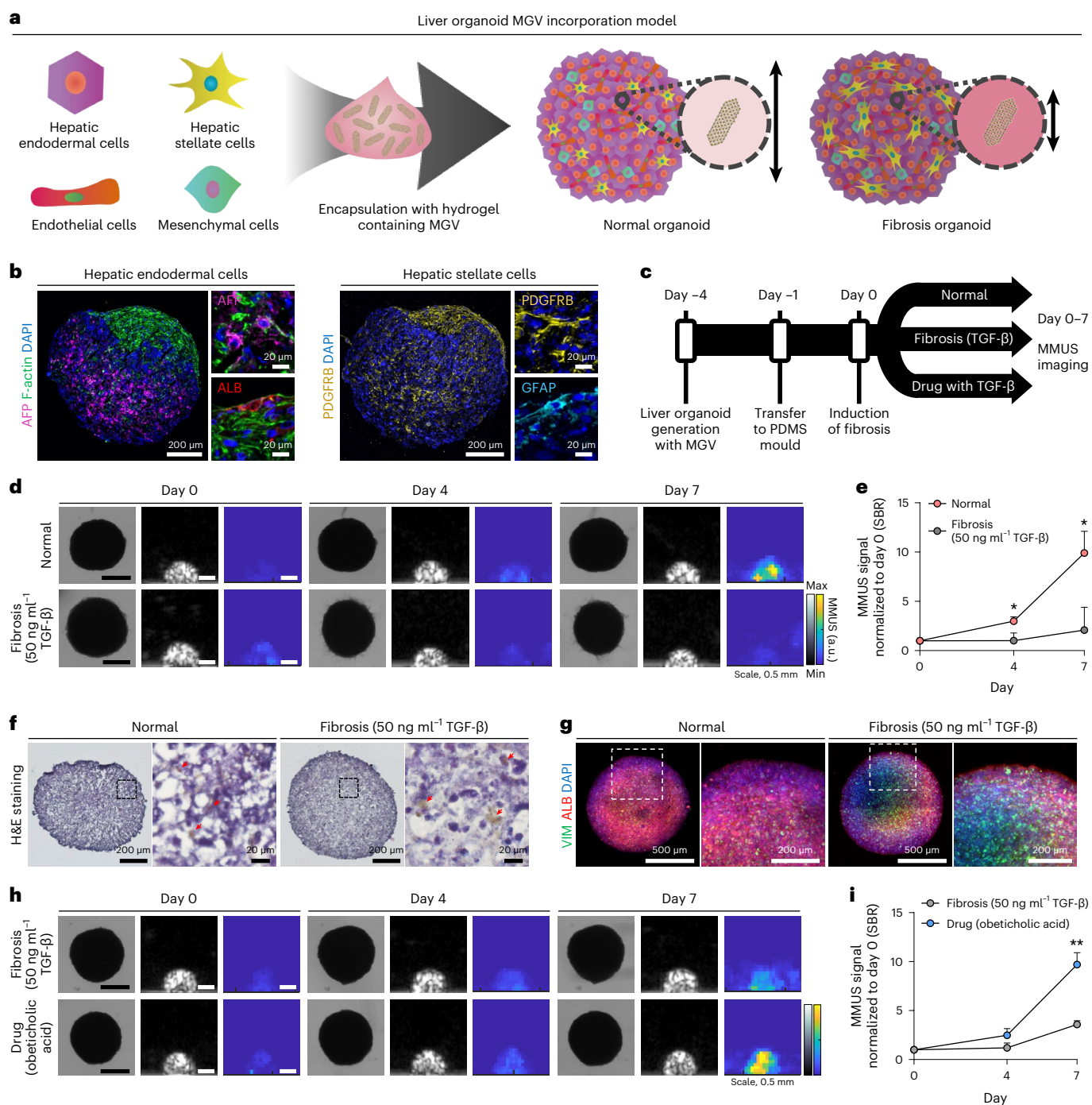


Fig. 4 | MGV-based MMUS imaging for monitoring fibrosis in human liver organoid models. **a**, Schematic illustration showing MGV encapsulation with four types of cells generating liver organoids and detecting fibrosis-related stiffness changes using MGVs. **b**, Immunofluorescent images showing the expression of hepatic endothelial cell markers (AFP and ALB) and hepatic stellate cell markers (PDGFRB, GFAP) in liver organoids 3 days after organoid generation. TRITC-conjugated phalloidin was used for cytoskeleton (F-actin) staining and DAPI was used for nuclear staining. $n = 3$ biological replicates examined in one experiment. The stained signals are presented in pseudocolour. **c**, Experimental timeline of the preparation of MGV-incorporated liver organoid models and MMUS imaging. **d**, **e** Bright-field, B-mode, MMUS images (**d**) and SBR quantification (**e**) of MGV-incorporated liver organoids (normal and fibrosis model). Images were taken from day 0 to day 7 after fibrosis induction. Quantification was conducted using relative MMUS SBR signal normalized to the day 0 value in normal and fibrosis groups. P (day 4-7) = 0.017975, 0.013180. $n = 3$ biological replicates examined in two experiments. **f**, H&E staining of organoid

sections in normal and fibrosis groups. Red arrows indicate the localization of MGVs in the organoids. $n = 2$ biological replicates examined in two experiments. **g**, Immunofluorescent images of fibrotic marker (VIM) and mature hepatic marker (ALB) in normal and fibrosis groups. DAPI was used for nuclear staining. $n = 2$ biological replicates examined in two experiments. **h**, **i**, Bright-field, B-mode, MMUS images (**h**) and SBR quantification (**i**) of MGV-incorporated liver organoids in the fibrosis group (50 ng ml $^{-1}$ TGF- β) and drug-treated fibrosis group (50 ng ml $^{-1}$ TGF- β + 10 μ M obeticholic acid). Images were taken from day 0 to day 7 after fibrosis induction. Quantification was conducted using relative MMUS SBR signal normalized to the day 0 value in fibrosis and drug-treated fibrosis groups. P (day 4-7) = 0.057215, 0.001129. $n = 3$ biological replicates examined in one experiment. Min and max on the parula (MMUS) and grey (B-mode) colour bars represent 0 and 20,000 arbitrary units. All lines and error bars represent mean \pm s.d., and significance was determined using an unpaired two-sided t -test in **e**, **i**: * $P < 0.05$, ** $P < 0.01$.

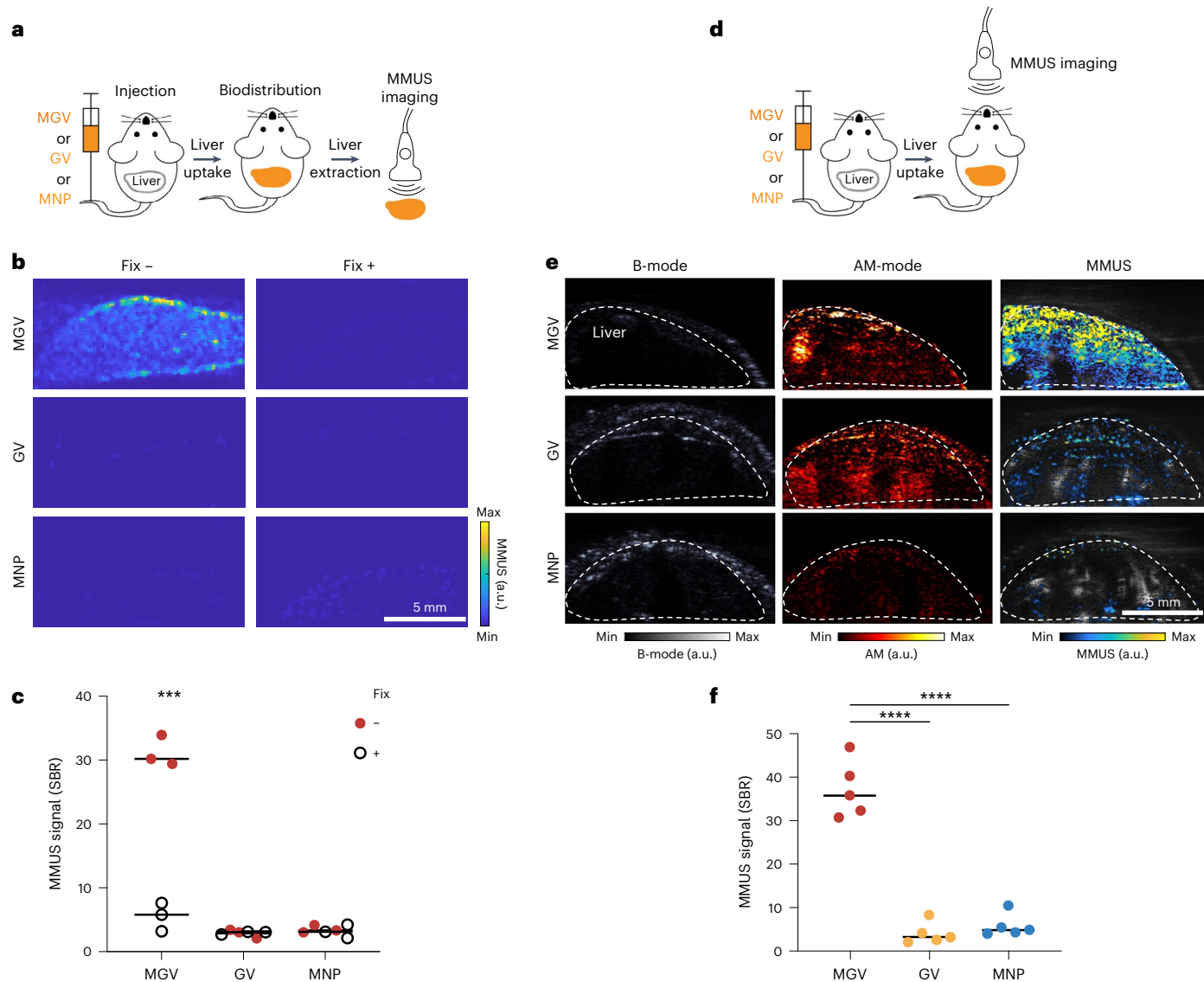


Fig. 5 | MGV-based MMUS imaging in mouse liver. **a**, Experimental scheme of ex vivo liver MMUS imaging. **b**, **c**, Ex vivo liver MMUS imaging (**b**) and SBR quantification (**c**) before and after fixation. MGVs, GVs or MNPs were injected into the tail vein of mice, and the liver was extracted 5 min after the initial injection. After the first round of imaging, the liver was fixed with 10% formalin for 48 h and imaged again. $P = 0.000178$. $n = 3$ animals per group. **d**, Experimental scheme of in vivo liver MMUS imaging. **e**, **f**, In vivo liver ultrasound images (**e**) and SBR quantification (**f**) of live animals. Three different nanomaterials (MGVs, GVs or MNPs) were injected intravenously and MMUS images were taken after 5 min. B-mode images reveal the position of the liver, AM images show the GV signal inside the liver and Δ MMUS images (parula scale) were overlapped

with Doppler images (grey scale) to show the signal below the skin. P (left–right) = 0.00000012, 0.00000022. $n = 5$ animals per group. In **b** min and max on the colour bar represent between 0 and 10,000 arbitrary units; in **e** min and max on the parula (MMUS) and hot (AM-mode) colour bars represent between 0 and 500,000 arbitrary units, respectively, and the grey (B-mode) colour bar represent between 0 and 1,000,000 arbitrary units. Each data point represents biologically independent animals, and lines represent the median of each group. Significance was determined using multiple unpaired two-sided t -test with Welch’s correction within each group (**c**) and one-way ANOVA with Tukey’s multiple comparisons (**f**): * $P < 0.05$, ** $P < 0.01$, *** $P < 0.001$, **** $P < 0.0001$.

we set out to test the ability of MGVs to produce robust ultrasound signals that can be visualized in deep tissues by MMUS imaging to image an in vivo biological process within live, breathing animals (Fig. 5d). This is an important challenge in non-invasive, deep-tissue imaging of tissue mechanics as it is well-documented that motion artefacts of live animals reduce accuracy and sensitivity⁴¹. After intravenous administration, both GVs and MGVs showed enhanced signals in AM images, confirming their delivery into the liver, while MNPs did not produce any detectable signals in vivo. We found that the mean MMUS signal of MGVs ($SBR = 37.1 \pm 6.5$) was 9.3-fold and 6.4-fold stronger than that of GVs (4.0 ± 2.4) and MNPs (5.8 ± 2.6), respectively (Fig. 5e,f). These results demonstrate that MGVs can be used as MMUS contrast agents

to improve signal strength and imaging sensitivity in more complex in vivo models.

Detection of liver fibrosis using MGVs

After establishing MGVs as excellent contrast agents for in vivo MMUS imaging, we then investigated whether our MGV-based system could function as a stiffness sensor to diagnose in vivo disease models. To induce liver fibrosis in mice, we injected CCl_4 , which increases hepatic stiffness during the progression of fibrosis for 30 days post-injection⁴². After 4 weeks of CCl_4 treatment, MMUS imaging was performed to assess the mechanical properties of fibrotic and normal livers (Fig. 6a). Intravenously administered MGVs were taken up by liver tissues and

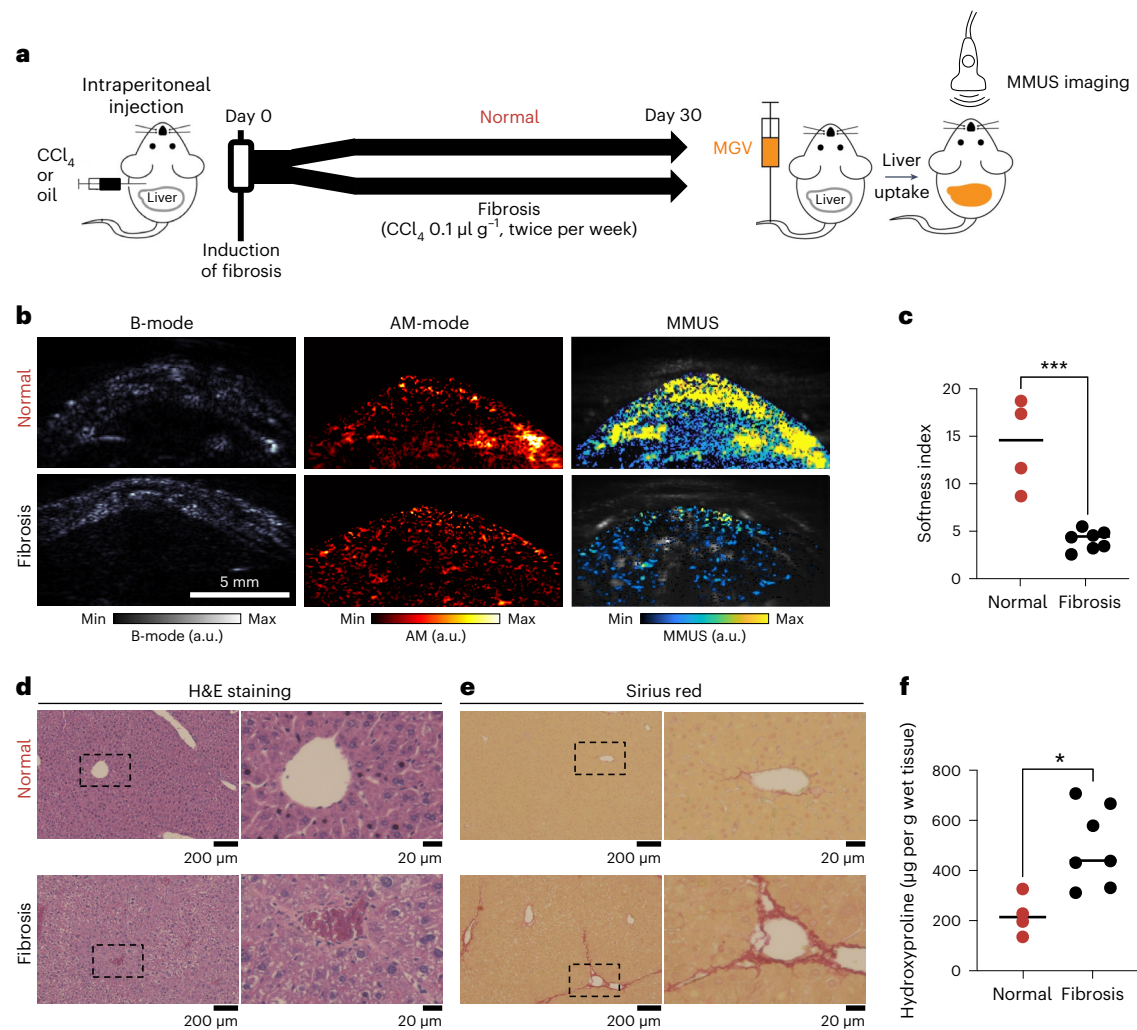


Fig. 6 | MGv-based MMUS imaging for in vivo fibrosis detection.

a, Experimental timeline of inducing liver fibrosis in a mouse model. Either CCl_4 or mineral oil at a volume of $0.1 \mu\text{l per g}$ (body weight) was injected intraperitoneally twice a week for up to 4 weeks. **b, c**, Ultrasound images (**b**) and SBR quantification (**c**) of normal and fibrosis cohorts. The B-mode images reveal the position of the liver, AM images show the GV signal inside the liver, and the Δ MMUS images (parula) were overlapped with Doppler images (grey) to show the signal below the skin. $P = 0.00033411$. $n = 4$ for normal group, $n = 7$ for fibrosis group. **d**, Low-magnification (left) and high-magnification (right) images of H&E-stained sections in two groups. $n = 3$ animals per group. **e**, Low-magnification

(left) and high-magnification (right) images of Sirius-red-stained sections in two groups. $n = 3$ animals per group. **f**, Quantification of the hydroxyproline content in liver from two groups. $P = 0.0111$. $n = 4$ for normal group, $n = 7$ for fibrosis group. In **b** min and max on the parula (MMUS) and hot (AM-mode) colour bars represent 0 and 500,000, respectively, and the grey (B-mode) colour bar ranges from 0 to 1,000,000 arbitrary units. Each data point represents biologically independent animals, and lines represent the median of each group. Significance was determined using an unpaired two-sided t -test: * $P < 0.05$, ** $P < 0.01$, *** $P < 0.001$, **** $P < 0.0001$.

retained their ultrasound scattering property, as evidenced by robust ultrasound contrast under AM. Although AM imaging confirmed that similar quantities of MGVs were delivered to the livers of both control and fibrotic mice, we observed a substantial reduction in MMUS signal in the fibrosis-induced cohort (Fig. 6b). A softness index, which we used as a quantitative indicator of in vivo tissue stiffness based on MMUS and AM imaging, was significantly lower in the fibrosis group (4.2 ± 1.0) than in normal controls (14.0 ± 4.6) (Fig. 6c), consistent with previous observations that liver stiffness increases with the progression of fibrosis⁴³. Histological and biochemical analyses confirmed the induction of liver fibrosis, as evidenced by pronounced morphological alteration, disruption of tissue architecture, fibre extension and increased collagen accumulation (Fig. 6d–f and Supplementary Fig. 11). No signs of fibrosis, inflammation and immune response were observed in animals injected with MGVs, suggesting these vesicles have high biocompatibility and negligible immunogenicity (Fig. 6d–f and Supplementary Fig. 9b,c). By utilizing clinically relevant ultrasound frequencies

(6.25 MHz) and biocompatible superparamagnetic iron oxide nanoparticles, we could also demonstrate the clinical potential of our MGv-based system (Supplementary Figs. 12 and 13). Moreover, organoid and liver tissue modulus could be estimated by correlating MGv concentration with B-mode and MMUS signals to make our system comparable across models (Supplementary Fig. 14a–e and Supplementary Note 2). These results demonstrate the potential of MGVs to serve as contrast agents for non-invasive detection of mechanical changes in vivo.

Outlook

Our results establish a new class of hybrid protein nanostructures (MGVs) as nanomaterial-based, magneto-acoustically modulated MMUS contrast agents for non-invasive and sensitive imaging and measurement of tissue elasticity in vivo. The clinical potential of MGv-based MMUS imaging for ultrasound-imaging-based diagnosis and drug screening of a wide range of diseases, including fibrosis, has been demonstrated. Our MGv-based MMUS imaging technique

provides several advantages over microbubble-based monitoring and other techniques, such as MRI, in disease monitoring^{44–47}. It offers wider availability, lower cost and improved stability and tissue accessibility, making it suitable for cost-effective and long-term disease monitoring. Improvements in magnetic field gradients, quantifiability and integration with existing strongly magnetic instruments such as MRI or magnetic particle imaging should make it possible to enhance the widespread use of MGV-based imaging. Moreover, the use of MGVs in stem-cell-derived organoid systems will offer a valuable tool for investigating mechanical properties and enable tissue-mechanics-based diagnosis and prediction of therapeutic outcomes in human diseases.

Online content

Any methods, additional references, Nature Portfolio reporting summaries, source data, extended data, supplementary information, acknowledgements, peer review information; details of author contributions and competing interests; and statements of data and code availability are available at <https://doi.org/10.1038/s41563-023-01688-w>.

References

- Martinez-Vidal, L. et al. Causal contributors to tissue stiffness and clinical relevance in urology. *Commun. Biol.* **4**, 1–16 (2021).
- Lee, W. et al. Dispersible hydrogel force sensors reveal patterns of solid mechanical stress in multicellular spheroid cultures. *Nat. Commun.* **2019** *10*:1 **10**, 144 (2019).
- Babu, P. K. V. & Radmacher, M. Mechanics of brain tissues studied by atomic force microscopy: a perspective. *Front Neurosci.* **13**, 600 (2019).
- Janmey, P. A., Fletcher, D. A. & Reinhart-King, C. A. Stiffness sensing by cells. *Physiol. Rev.* **100**, 695–724 (2020).
- Gayraud, C. & Borghi, N. FRET-based molecular tension microscopy. *Methods* **94**, 33–42 (2016).
- Lekka, M., Gnanachandran, K., Kubiak, A., Zieliński, T. & Zemła, J. Traction force microscopy—measuring the forces exerted by cells. *Micron* **150**, 103138 (2021).
- Schroyen, B., Vlassopoulos, D., Van Puyvelde, P. & Vermant, J. Bulk rheometry at high frequencies: a review of experimental approaches. *Rheol. Acta* **59**, 1–22 (2020).
- Kabel, J., Edwards, T. E. J., Sharma, A., Michler, J. & Hosemann, P. Direct observation of the elasticity–texture relationship in pyrolytic carbon via in situ micropillar compression and digital image correlation. *Carbon NY* **182**, 571–584 (2021).
- Bruce, M., Kolokythas, O., Ferraioli, G., Filice, C. & O'Donnell, M. Limitations and artifacts in shear-wave elastography of the liver. *Biomed. Eng. Lett.* **7**, 81–89 (2017).
- Campàs, O. et al. Quantifying cell-generated mechanical forces within living embryonic tissues. *Nat. Methods* **11**, 183–189 (2014).
- Serwane, F. et al. In vivo quantification of spatially-varying mechanical properties in developing tissues. *Nat. Methods* **14**, 181–186 (2017).
- Mok, S. et al. Mapping cellular-scale internal mechanics in 3D tissues with thermally responsive hydrogel probes. *Nat. Commun.* **11**, 4757 (2020).
- Mantha, S. et al. Smart hydrogels in tissue engineering and regenerative medicine. *Materials* **12**, 3323 (2019).
- Sjöstrand, S., Evertsson, M. & Jansson, T. Magnetomotive ultrasound imaging systems: basic principles and first applications. *Ultrasound Med. Biol.* **46**, 2636–2650 (2020).
- Levy, B. E. et al. Effect of model thrombus volume and elastic modulus on magnetomotive ultrasound signal under pulsatile flow. *IEEE Trans. Ultrason. Ferroelectr. Freq. Control* **65**, 1380–1388 (2018).
- Sjöstrand, S. et al. Contrast-enhanced magnetomotive ultrasound imaging (CE-MMUS) for colorectal cancer staging: assessment of sensitivity and resolution to detect alterations in tissue stiffness. *2019 IEEE International Ultrasonics Symposium (IUS)*, Glasgow, 1077–1080 (2019); <https://doi.org/10.1109/ULTSYM.2019.8926058>
- Farhadi, A., Ho, G. H., Sawyer, D. P., Bourdeau, R. W. & Shapiro, M. G. Ultrasound imaging of gene expression in mammalian cells. *Science* **365**, 1469–1475 (2019).
- Hurt, R. C. et al. Genomically mined acoustic reporter genes for real-time in vivo monitoring of tumors and tumor-homing bacteria. *Nat. Biotechnol.* <https://doi.org/10.1038/s41587-022-01581-y> (2023).
- Shapiro, M. G. et al. Biogenic gas nanostructures as ultrasonic molecular reporters. *Nat. Nanotechnol.* **9**, 311–316 (2014).
- Kim, J. et al. Single-cell mechanogenetics using monovalent magnetoplasmonic nanoparticles. *Nat. Protoc.* **12**, 1871–1889 (2017).
- Lu, G. J. et al. Acoustically modulated magnetic resonance imaging of gas-filled protein nanostructures. *Nat. Mater.* **17**, 456–463 (2018).
- Tse, J. R. & Engler, A. J. Preparation of hydrogel substrates with tunable mechanical properties. *Curr. Protoc. Cell Biol.* **47**, 10.16.1–10.16.16 (2010).
- Holmes, D. L. & Stellwagen, N. C. Estimation of polyacrylamide gel pore size from Ferguson plots of normal and anomalously migrating DNA fragments. I. Gels containing 3% *N,N*'-methylenebisacrylamide. *Electrophoresis* **12**, 253–263 (1991).
- Kim, J., Koo, B.-K. & Knoblich, J. A. Human organoids: model systems for human biology and medicine. *Nat. Rev. Mol. Cell Biol.* **21**, 571–584 (2020).
- Kang, H. J. et al. Cereblon contributes to the development of pulmonary fibrosis via inactivation of adenosine monophosphate-activated protein kinase α 1. *Exp. Mol. Med.* **53**, 885–893 (2021).
- Meng, X., Nikolic-Paterson, D. J. & Lan, H. Y. TGF- β : the master regulator of fibrosis. *Nat. Rev. Nephrol.* **12**, 325–338 (2016).
- Seki, E. et al. TLR4 enhances TGF- β signaling and hepatic fibrosis. *Nat. Med.* **13**, 1324–1332 (2007).
- Jonsdottir, H. R. et al. Basal cells of the human airways acquire mesenchymal traits in idiopathic pulmonary fibrosis and in culture. *Lab. Invest.* **95**, 1418–1428 (2015).
- Wollin, L. et al. Mode of action of nintedanib in the treatment of idiopathic pulmonary fibrosis. *Eur. Respir. J.* **45**, 1434–1445 (2015).
- Chen, G. et al. Matrix mechanics as regulatory factors and therapeutic targets in hepatic fibrosis. *Int. J. Biol. Sci.* **15**, 2509–2521 (2019).
- Lachowski, D. et al. Matrix stiffness modulates the activity of MMP-9 and TIMP-1 in hepatic stellate cells to perpetuate fibrosis. *Sci. Rep.* **9**, 1–9 (2019).
- Daley, W. P., Peters, S. B. & Larsen, M. Extracellular matrix dynamics in development and regenerative medicine. *J. Cell Sci.* **121**, 255–264 (2008).
- Bonnans, C., Chou, J. & Werb, Z. Remodelling the extracellular matrix in development and disease. *Nat. Rev. Mol. Cell Biol.* **15**, 786–801 (2014).
- Margagliotti, S. et al. Role of metalloproteinases at the onset of liver development. *Dev. Growth Differ.* **50**, 331–338 (2008).
- Roeb, E. Matrix metalloproteinases and liver fibrosis (translational aspects). *Matrix Biol.* **68–69**, 463–473 (2018).
- Radbill, B. D. et al. Loss of matrix metalloproteinase-2 amplifies murine toxin-induced liver fibrosis by upregulating collagen I expression. *Dig. Dis. Sci.* **56**, 406–416 (2011).
- Maresca, D., Sawyer, D. P., Renaud, G., Lee-Gosselin, A. & Shapiro, M. G. Nonlinear X-wave ultrasound imaging of acoustic biomolecules. *Phys. Rev. X* **8**, 041002 (2018).
- Rabut, C. et al. Ultrafast amplitude modulation for molecular and hemodynamic ultrasound imaging. *Appl Phys. Lett.* **118**, 244102 (2021).

39. Ling, B. et al. Biomolecular ultrasound imaging of phagolysosomal function. *ACS Nano* **14**, 12210–12221 (2020).
40. Ling, Y. et al. Effects of fixation and preservation on tissue elastic properties measured by quantitative optical coherence elastography (OCE). *J. Biomech.* **49**, 1009–1015 (2016).
41. Chen, Q., Song, H., Yu, J. & Kim, K. Current development and applications of super-resolution ultrasound imaging. *Sens. (Basel)* **21**, 2417 (2021).
42. Delire, B., Stärkel, P. & Leclercq, I. Animal models for fibrotic liver diseases: what we have, what we need, and what is under development. *J. Clin. Transl. Hepatol.* **3**, 53 (2015).
43. Georges, P. C. et al. Increased stiffness of the rat liver precedes matrix deposition: implications for fibrosis. *Am. J. Physiol. Gastrointest. Liver Physiol.* **293**, 1147–1154 (2007).
44. Vorobiev, V. et al. Vascular-targeted micelles as a specific MRI contrast agent for molecular imaging of fibrin clots and cancer cells. *Eur. J. Pharm. Biopharm.* **158**, 347–358 (2021).
45. Shuvaev, S., Akam, E. & Caravan, P. Molecular MR contrast agents. *Invest. Radio.* **56**, 20–34 (2021).
46. Beguin, E., Bau, L., Shrivastava, S. & Stride, E. Comparing strategies for magnetic functionalization of microbubbles. *ACS Appl Mater. Interfaces* **11**, 1829–1840 (2019).
47. Owen, J. et al. Magnetic targeting of microbubbles against physiologically relevant flow conditions. *Interface Focus* **5**, 1–12 (2015).

Publisher's note Springer Nature remains neutral with regard to jurisdictional claims in published maps and institutional affiliations.

Open Access This article is licensed under a Creative Commons Attribution 4.0 International License, which permits use, sharing, adaptation, distribution and reproduction in any medium or format, as long as you give appropriate credit to the original author(s) and the source, provide a link to the Creative Commons license, and indicate if changes were made. The images or other third party material in this article are included in the article's Creative Commons license, unless indicated otherwise in a credit line to the material. If material is not included in the article's Creative Commons license and your intended use is not permitted by statutory regulation or exceeds the permitted use, you will need to obtain permission directly from the copyright holder. To view a copy of this license, visit <http://creativecommons.org/licenses/by/4.0/>.

© The Author(s) 2023

Methods

All experiments were performed in accordance with relevant guidelines and ethical regulations that were approved. The use of human lung tissues for lung organoid generation was approved by the Institutional Review Board (IRB) of Severance Hospital (IRB number 4-2021-1555). Tissue fragments were collected from patients undergoing lung surgery after obtaining their informed consent. A human-induced pluripotent stem cell (hiPSC) line (CHO) was kindly provided by the Yonsei University School of Medicine, and the use of hiPSCs for the liver organoid study was approved by the IRB of Yonsei University (permit numbers 7001988-202104-BR-1174-01E, 7001988-202104-BR-1175-01E). All in vivo experiments were conducted in accordance with protocol 1735 approved by the California Institute of Technology's Institutional Animal Care and Use Committee.

Preparation of MNPs

Zinc-doped iron oxide ($\text{Zn}_{0.4}\text{Fe}_{2.6}\text{O}_4$) nanoparticles were synthesized by previously published procedures²⁰. To synthesize zinc-doped iron oxide ($\text{Zn}_{0.4}\text{Fe}_{2.6}\text{O}_4$) nanoparticles, 0.6 g of zinc(II) chloride (ZnCl_2 , $\geq 98\%$, Sigma-Aldrich) and 1.756 g iron(III) acetylacetonate ($\text{Fe}(\text{acac})_3$, $\geq 98\%$, Sigma-Aldrich) were placed in a three-neck round-bottom flask in the presence of 5 ml of oleic acid (Sigma-Aldrich), 20 ml of oleylamine (Sigma-Aldrich) and 20 ml of trioctylamine (98%, Sigma-Aldrich) under argon gas. After the synthesis, the precipitation and washing were performed using ethanol and toluene. Silica coating was used to make these nanoparticles water soluble and functionalizable. To begin, for 1 mg of MNPs the surface was treated with 10 μl of tetraethyl orthosilicate (Sigma-Aldrich), 12.6 ml of cyclohexane (Deajung), 786 mg of IGEAL CO-520 (Sigma-Aldrich) and 105 μl of ammonium hydroxide solution (28%, Sigma-Aldrich) for 24 h at room temperature. The second layer was coated with 6 μl of 3-aminopropyl trimethoxysilane (Sigma-Aldrich) for 2 h. After separation with tetramethyl ammonium hydroxide (TMAOH, 97%, Sigma-Aldrich), to introduce azide groups on the surface of the nanoparticles, silica-coated nanoparticles (1 mg) were then coated with m-dPEG12-TFP ester (9 mg, Quanta BioDesign), azido-dPEG12-TFP ester (1 mg, Quanta BioDesign) in dimethylsulfoxide for 2 h at room temperature. Nanoparticles were isolated using a MidiMACS separator column and were dispersed in 10 mM phosphate buffer.

Preparation of GVs

Anabaena gas vesicles were obtained according to published procedures⁴⁸. GVs were isolated from *A. flos-aquae* using hypertonic lysis and purified using centrifugally assisted flotation. Stripped GVs were prepared by treatment with 6 M urea solution followed by an additional centrifugally assisted flotation and removal of the supernatant. To functionalize DBCO on the surface of the GVs, DBCO-sulfo-NHS ester (Click Chemistry Tool) was mixed with GVs at a molar ratio of 1:10 in deionized water (DIW) for 4 h at 4 °C at 30 r.p.m. in a vertical shaker. Functionalized GVs were dialysed in DIW for 72 h with a water exchange every 24 h.

Development and characterization of MGVs

MGVs were developed by conjugating MNPs to GVs at a molar ratio of 1:100 for 4 h at 4 °C at 30 r.p.m. in a vertical shaker. After 4 h, the MGVs were purified three times using buoyancy purification at 300g, 4 °C, 24 h, and the solvent was replaced with phosphate-buffered saline (PBS) each time. We characterized the morphology, size and magnetic susceptibility of MGVs by transmission electron microscopy (TEM, JEOL 2100, DigitalMicrograph 3.22.1461.0, JEOL), dynamic light scattering (Zetasizer Nano ZS, software 7.12) and vibrating-sample magnetometry (Vibration 7407-S, software 4.9.0, Lake Shore Cryotronics), respectively. ICPMS (ICAP 7200 Duo + ASX-560, Qtegra 2.6.2270, Thermo Fisher Scientific) was used to determine the concentration of MNPs in MGVs. The concentrations of iron and zinc ions measured by ICPMS were converted to numbers of MNPs. The concentration of GVs

was then calculated by dividing 186 by the average number of MNPs attached to GVs as determined by our TEM images, which was manually calculated (Supplementary Fig. 3).

Experimental MMUS imaging set-up

Magnet set-up. A schematic illustration of our custom-built MMUS system is illustrated in Fig. 1a. A multipurpose data-acquisition module (USB6003, National Instruments), power supply (RSP-1000-24, 24 V, 40 A, Meanwell) and solid-state module (SSR-40DD, FOTEK) were commercially available items. To meet the imaging system requirements, the ultrasound system was modified to output a trigger signal prior to imaging to generate a magnetic field. The magnetic field pulse and strength were controlled by using a customized LabVIEW system. The field generator was connected to a coil consisting of multiple turns with a magnetic coil. To increase the magnetic flux density and to localize the magnetic field in the centre of the coil, ferritic stainless steel was embedded. The core size was 5 mm in diameter and 100 mm in height. To better focus the field onto a smaller region of interest, a symmetric conic frustum was cut at 56° on the top side. The magnetic pulse strength, measured at 6 mm above the iron-core tip using a digital gaussmeter (DSP 475, Lakeshore Inc., Westerville, OH), was 0.03 T, which was used for the imaging experiments. Different magnetic strengths were achieved by adjusting the distance between the sample and the magnet.

MMUS imaging and processing. For MMUS imaging, the phantoms were submerged in PBS, and ultrasound images were acquired using a Verasonics Vantage programmable ultrasound scanning system with an L22-14v 128-element linear array transducer with a 0.10 mm pitch, an 8 mm elevation focus, a 1.5 mm elevation aperture and a centre frequency of 15.6 MHz with 67%–6 dB bandwidth (Verasonics). Measured peak voltages received by the transducer were collected as I/Q data. Two sets of ultrasound I/Q data were collected for in vitro and organoid imaging at each loop containing a pulse sequence consisting of five tilted plane waves (varying from -6° to 6°), each containing 500 ensemble coherently compounded frames, collected at a frame rate of 500 Hz with a voltage of 3 V. A total of 20 loops of images were collected per set. The first set was taken as a background frame for background subtraction with the magnetic field off (Mag OFF). The second set was taken with the magnetic field on (Mag ON), during which the function generator was triggered for 2,000 μs prior to the beginning of the imaging.

To obtain each image, I/Q data were processed with quadrature detection used to extract the generated movement based on the excitation frequency⁴⁹. Briefly, for a set of N frames, let $R_i(x, y, n) + jR_q(x, y, n)$ represent an element in this I/Q array with n running from 1 to N , and R_i and R_q representing the in-phase and quadrature signal, respectively. First, the received I/Q data were phase unwrapped to generate a new 3D array $r_{\text{unwrapped}}(x, y, n) = \arg(R_i(x, y, n) + jR_q(x, y, n))$. Then, quadrature detection was used to tease out the signal that oscillates at the magnetic pulse frequency (f_0)

$$R(x, y, n) = r_{\text{unwrapped}}(x, y, n) \times e^{j \times 2\pi \times f_0 \times n \times \Delta t}$$

To calculate the displacement amplitude at frequency f_0 for each pixel, all the frames were averaged to calculate $R(x, y)$ for the quadrature-detected sequence $R(x, y, n)$. The mean value was used rather than a low-pass filter to determine the displacement amplitude at f_0 , which was obtained as

$$A(x, y) = 2|R(x, y)| = 2\sqrt{I(x, y)^2 + Q(x, y)^2}$$

Finally, ultrasound Δ images were constructed by subtracting the Mag OFF frame from the Mag ON frame. Regions of interest (ROIs)

were defined to capture the ultrasound signal from the phantom well or organoid region on various images such as MMUS (Δ), B-mode or cross-propagating amplitude modulation (xAM) images. All in vitro phantom experiments had the same ROI dimensions. For organoid models, ROIs were selected in B-mode images in which the organoid size was not same in all cases. Background ROIs were chosen in areas where no sample was present. The mean pixel intensity was calculated for each ROI, and the signal from the background region and the sample region was calculated as the SBR.

Ultrasound phantom preparation

In vitro phantom. To produce in vitro MMUS imaging phantoms, wells were cast with molten 0.5% (w/v) agarose in PBS using a custom 3D-printed template⁴⁸. MGv, MNP or GV (DBCO-functionalized GV) samples were mixed 1:1 with 50 °C agarose and injected into wells prior to solidification. Matrigel was stored at 4 °C until loaded and solidified for 30 min at 37 °C. Agarose or Matrigel hydrogels and samples were made at a concentration two times greater than the final required concentration. For polyacrylamide gels, the desired concentrations of acrylamide and bis-acrylamide were combined with 0.002 M lithium phenyl-2,4,6-trimethylbenzoylphosphinate solution dissolved in DIW (Supplementary Table 1). After the combination, these gels were cast in a custom 3D-printed template. The MGv concentration was 20 times greater than the final required concentration and was mixed 1:20 with polyacrylamide solutions before being cast into each well. The gels were solidified for 5 min with an ultraviolet lamp (DR-301C, MelodySusie).

Organoid phantom. For MMUS imaging of organoids, a PDMS mould was fabricated. PDMS solution was prepared by mixing PDMS prepolymer (Sylgard 184; Dow Corning) and curing agent (Dow Corning) at a ratio of 10:1 (v/v). Then the mixture was poured into 60 mm Petri dishes and cured in a drying oven for 4 h after removing bubbles using a vacuum chamber. The centre of the cured PDMS mould was punched to make chambers for the organoids. After sterilizing each PDMS mould with ultraviolet irradiation for 30 min, MGv-microinjected lung organoids or MGv-incorporated liver organoids were encapsulated in growth-factor-reduced Matrigel (Corning) and transferred to the chambers in the mould. After the gelation of Matrigel, the organoids were cultured in growth medium, and MMUS imaging was performed after replacing the medium with 1× PBS (Sigma-Aldrich). For fibrosis induction, lung organoids were cultured in medium including recombinant human TGF- β 1 (Peprotech) without A83-01 (Tocris). For the drug tests with lung organoids, 10 μ M nintedanib (Sigma-Aldrich) was administered to the organoids every 2–3 days starting from day 5 after fibrosis induction. Liver organoids were also cultured in medium containing TGF- β 1 for fibrosis induction, and 10 μ M obeticholic acid (Selleck) used for the drug tests was administered to the organoids every 2–3 days starting from the first day of fibrosis induction (day 0).

Generation of MGv organoids

Details of how the MGv-microinjected lung and MGv-incorporated liver organoids are generated are given in the Supplementary Information. Information on the maintenance and immunostaining of organoids is also given in the Supplementary Information. Chemicals for synthetic operations were purchased from common suppliers (Sigma-Aldrich, Thermo Fisher Scientific, Abcam, etc.) and were stored at the suitable temperatures.

Animal experiments

Animals were randomly assigned to experimental groups by the animal facilities. Animals were housed in a facility maintained at 71–75 °F and 30–70% humidity, with a lighting cycle of 13 h on and 11 h off (light cycle 6:00–19:00). Throughout all injection and imaging procedures, mice were anaesthetized with 1–2.5% isoflurane. Mice were positioned with the liver facing directly upwards. Prior to each experiment, ultrasound

gel was centrifuged at 2,000g for 10 min to remove bubbles, heated to 37 °C and then carefully applied to the bodies of the mice. To obtain a precise signal, for all ex vivo and in vivo models, stripped GVs were used. Stripped MGVs were prepared in the same manner as MGVs. The concentration of GVs was matched to the concentration of MGVs. MNP concentration was also matched to the MNP concentration found in the MGVs.

Ex vivo imaging. For ex vivo imaging, three C57 male mice aged 8 weeks were injected intravenously in the tail vein with 2,280 pM ($OD_{500} = 20$) of MGVs and were killed 5 min later. The concentration used for the injections was chosen based on previous research. After the animals had been killed, their livers were harvested for ex vivo imaging. For MMUS imaging, the liver was cast in 0.5% (w/v) agarose in a 100 mm Petri dish and solidified for 10 min. After the first series of imaging, the tissue was fixed for 48 h in 10% formalin at 4 °C. The second series of ex vivo imaging occurred after fixation.

Live animal imaging. Five 4-week-old C57 male mice were intravenously injected with MGVs for in vivo imaging. The regions of interest were positioned in the liver tissue using B-mode and Doppler anatomical imaging. The concentration used for injections was chosen based on previous research. MMUS imaging was performed before and after the injection of MGVs with the magnetic field on. MGVs (100 μ l at 2,280 pM ($OD_{500} = 20$)) were injected intravenously via the tail vein, and MMUS images were taken 5 min post-injection.

Fibrosis model. Prior to the in vivo fibrosis experiment, animals were randomized between experimental groups; blinding was not necessary. Four-week-old C57 male mice were treated with CCl_4 (1 μ l per g (body weight), 1:4 dilution with mineral oil, $n = 7$) or with mineral oil alone (1 μ l per g (body weight), $n = 4$) via intraperitoneal injection two times per week for 4 weeks^{50,51}. After 4 weeks, the ROIs were positioned in the liver tissue using B-mode and Doppler imaging. MMUS imaging was performed before and 5 min after injection with the magnetic field on. MGVs (2,280 pM) were injected intravenously via the tail vein in the normal and fibrosis model groups. After MMUS imaging, livers were harvested. Fresh tissue was homogenized and used for a hydroxyproline assay (Sigma-Aldrich). Other parts of the tissue were fixed for 24 h in 10% formalin and then submerged in 70% ethanol for storage. Next, the fixed tissue was embedded in paraffin, sectioned and stained with H&E and Sirius red (Abcam). The images were examined under a laser scanning confocal microscope (Zeiss LSM880, Jena, Germany) and analysed using Zen v.3.0 (Zeiss).

In vivo ultrasound imaging. We employed a recently developed method of uAM to precisely visualize and quantify ultrasound contrast in vivo³⁸. Due to the attenuation of applied sound waves caused by the body, we increased the sound pressure to 370 kPa with the same Verasonics system using an L22-14v transducer, which did not collapse either MGVs or GVs³⁸. For each loop, the data were collected at a frame rate of 350 Hz with a voltage of 6 V (370 kPa). The pulse sequence consisted of four bursts repeated at three different amplitudes with four different polarity patterns (varying from -14° to 14°). Each burst contained 500 ensemble coherently compounded frames. Two sets of images were taken prior to and following injection. The first set was used as a baseline for background subtraction purposes, with the magnetic field activated prior to injection (before). The second set was taken 5 min after injection with the magnetic field activated (after), with the function generator triggered 2,000 μ s prior to the start of imaging. A total of 20 looped images were collected per set. We removed frames with poor breathing artefacts based on their Doppler images. To obtain in vivo ultrasound images, the same processing procedures were used as in vitro ultrasound imaging, and ultimately, ultrasound Δ images were constructed by subtracting the after image from the

before image. For in vivo MMUS signal quantification, the Δ images were used. ROIs were selected consistently to exclude edge effects from the skin. Background ROIs were selected where there was no sample at all. The mean pixel intensity was calculated for each ROI, and the signal from the background region and sample region was calculated as the SBR. For the fibrosis experiments, the ratio of the MMUS (SBR) signal to the uAM (SBR) signal was calculated and reported as a softness index.

Statistics and reproducibility

All data are presented as box plots or line plots expressed as mean \pm s.d. unless otherwise indicated. The number of experiments and statistical comparisons are specified for each experiment and reported in the figure legends. Sample sizes were chosen on the basis of preliminary experiments to have sufficient replicates for statistical comparison. Data distribution was assumed to be normal but this was not formally tested. Statistical calculations were performed in GraphPad Prism 9. The microscopic and ultrasound images in the figures are representative images obtained from independent samples, biological replicates or biologically independent animals with similar results. No data were excluded from the analyses. The investigators were not blinded to allocation during experiments and outcome assessment unless otherwise indicated. For cell culture experiments, standardized cell culture conditions and samples used in each set of experiments were equal to minimize variation across samples, except the experimental condition being tested. Cultured lung and liver organoids were randomly assigned for each group when they reached each specified time point. For mouse experiments, animals were randomly assigned to experimental groups by the animal facilities and cages of animals were randomly chosen for the experimental groups versus control conditions. In all other experiments, samples were allocated randomly and performed with appropriate control.

Reporting summary

Further information on research design is available in the Nature Portfolio Reporting Summary linked to this article.

Data availability

The data presented in this study are available in the Source data. Additional information and requests for resources and reagents that support the findings of this study are available from the corresponding author upon reasonable request. Source data are provided with this paper.

Code availability

Ultrasound data acquisition and analysis code is available on the Shapiro laboratory GitHub at <https://github.com/shapiro-lab>.

References

48. Lakshmanan, A. et al. Preparation of biogenic gas vesicle nanostructures for use as contrast agents for ultrasound and MRI. *Nat. Protoc.* **12**, 2050–2080 (2017).
49. Evertsson, M. et al. Frequency- and phase-sensitive magnetomotive ultrasound imaging of superparamagnetic iron oxide nanoparticles. *IEEE Trans. Ultrason. Ferroelectr. Freq. Control* **60**, 481–491 (2013).
50. Wu, B.-M., Liu, J.-D., Li, Y.-H. & Li, J. Margatoxin mitigates CCl_4 -induced hepatic fibrosis in mice via macrophage polarization, cytokine secretion and STAT signaling. *Int. J. Mol. Med* **45**, 103–114 (2020).

51. Scholten, D., Trebicka, J., Liedtke, C. & Weiskirchen, R. The carbon tetrachloride model in mice. *Lab. Anim.* **49**, 4–11 (2015).

Acknowledgements

This work was supported by the Institute for Basic Science (IBS-R026-D1, to J.-H.L., M.K., S.-W.C. and J.C.). This work was also supported by a National Research Foundation of Korea (NRF) grant funded by the Korean government, the Ministry of Science and ICT (MSIT) (numbers 2021R1A2C3004262 and 2022M3A9B6082675) and Samsung Research Funding & Incubation Center of Samsung Electronics under project number SRFC-TC2003-03 to S.-W.C. This research was also supported by the Yonsei Signature Research Cluster Program of 2023-22-0012 and the Yonsei Fellow Program funded by Lee Youn Jae to S.-W.C. This work was also supported by the US National Institutes of Health (R01-EB018975) to M.G.S. E.C.-H. was supported by the James G. Boswell Fellowship in Molecular Engineering and MRI. M.G.S. is an Investigator of the Howard Hughes Medical Institute (HHMI).

This article is subject to HHMI's Open Access to Publications policy. HHMI Investigators have previously granted a non-exclusive CC BY 4.0 license to the public and a sublicensable license to HHMI in their research articles. Pursuant to those licenses, the author-accepted manuscript of this article can be made freely available under a CC BY 4.0 license immediately upon publication.

Author contributions

W.-S.K. performed overall in vitro and in vivo experiments and analysed data. S.M. designed and performed organoid-related experiments. S.K.K., Y.H.K. and S.A. supported hiPSC differentiation, MMUS imaging and hydrogel characterization, respectively. S.K. provided magnetic nanoparticles. E.C.-H. supported the measurements of ultrasound signals using hydrophones. H.D. and A.B.-Z. performed initial set-up and discussions on this research. D.M. provided gas vesicles. J.-H.L. helped with initial set-up and discussions on this research. S.H.B. and J.G.L. provided lung tissue for the organoid development. M.K. assisted with the design of research and experiment. W.-S.K. and M.K. wrote the manuscript with input from all authors. S.-W.C., M.G.S. and J.C. conceived and supervised the project.

Competing interests

The authors declare no competing interests.

Additional information

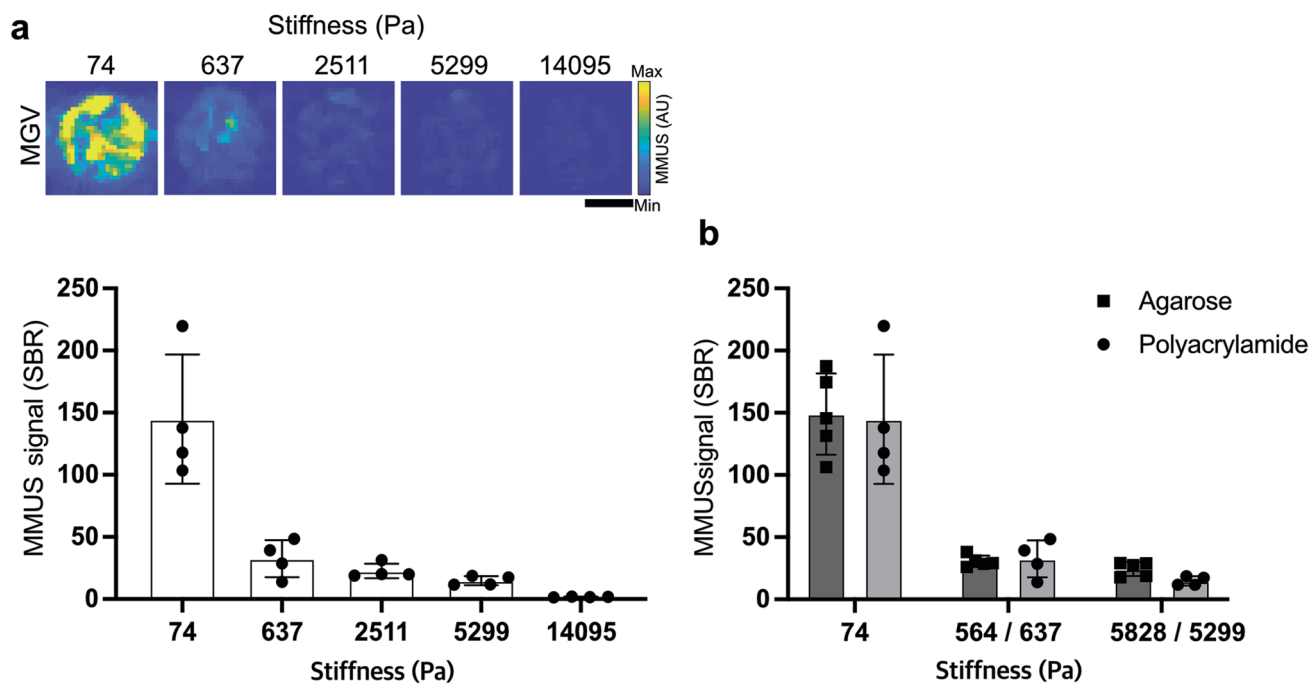
Extended data is available for this paper at <https://doi.org/10.1038/s41563-023-01688-w>.

Supplementary information The online version contains supplementary material available at <https://doi.org/10.1038/s41563-023-01688-w>.

Correspondence and requests for materials should be addressed to Seung-Woo Cho, Mikhail G. Shapiro or Jinwoo Cheon.

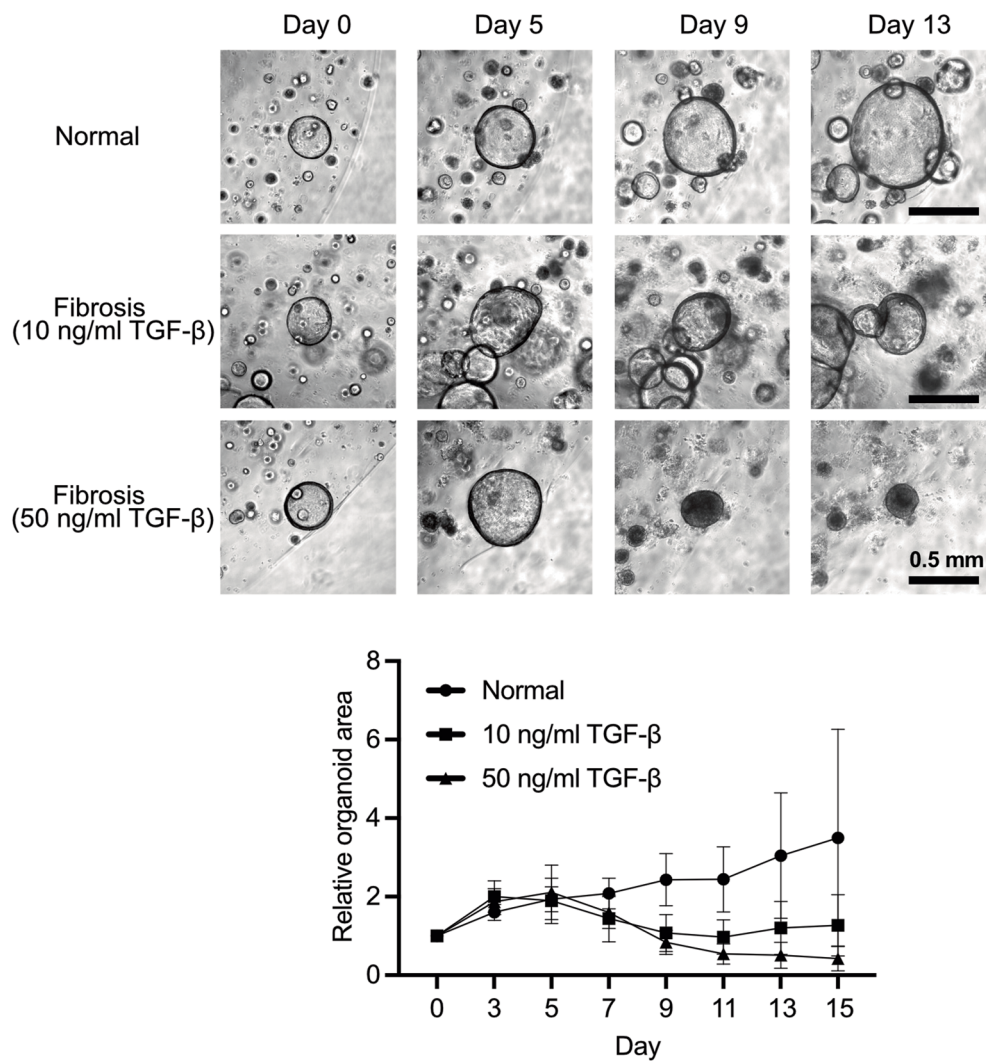
Peer review information *Nature Materials* thanks Jeff Bulte, Constantin Coussios and Christopher Moraes for their contribution to the peer review of this work.

Reprints and permissions information is available at www.nature.com/reprints.



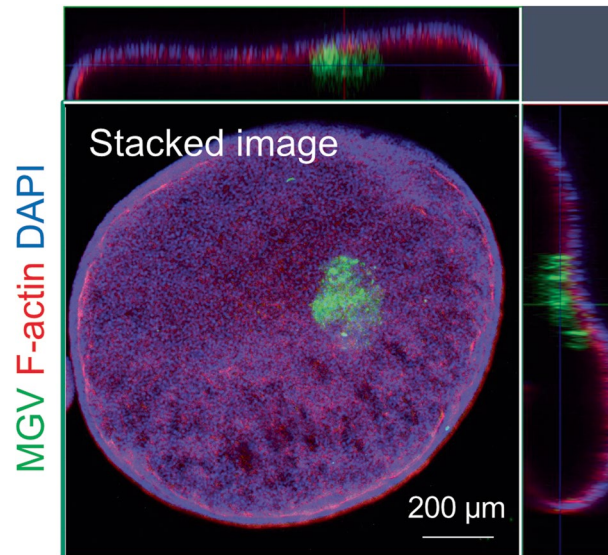
Extended Data Fig. 1 | Stiffness-dependent MMUS imaging in a polyacrylamide phantom. (a) MMUS images and SBR quantification of polyacrylamides with stiffnesses ranging from 74 Pa to 14,095 Pa. MMUS imaging was performed using 0.8 nM MGVs ($n = 4$ independent experiments). Min and max on color bars represent 0 and 10000 arbitrary units, respectively. Scale

bars, 1 mm. (b) Comparison of the MMUS signal quantification (SBR) in different hydrogels of similar stiffness ($n = 5$ for agarose, $n = 4$ for polyacrylamide). All points represent independent experiments, and line and error bars represent mean \pm s.d.

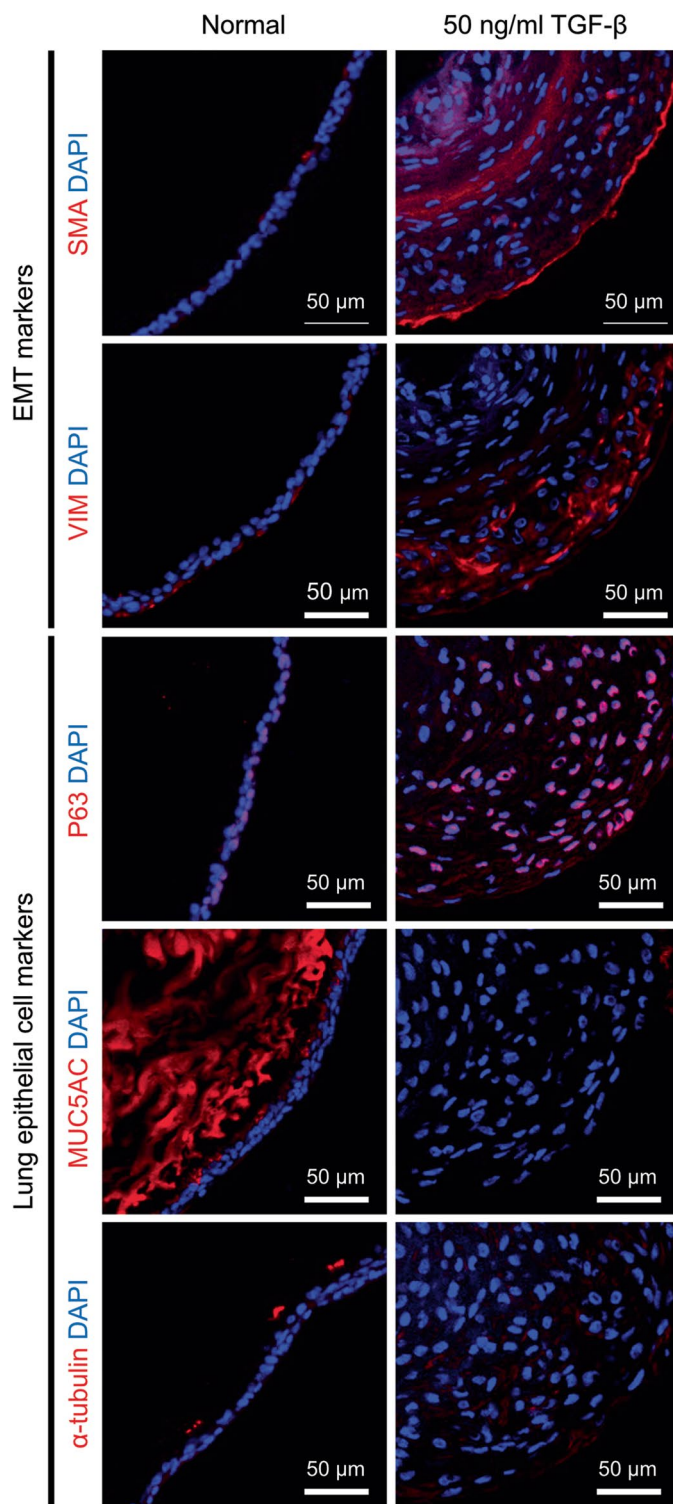


Extended Data Fig. 2 | Tracking the fibrotic response of lung organoids during culture. Bright-field images and size quantification graph of lung organoids composed of one normal model and two fibrosis models treated with

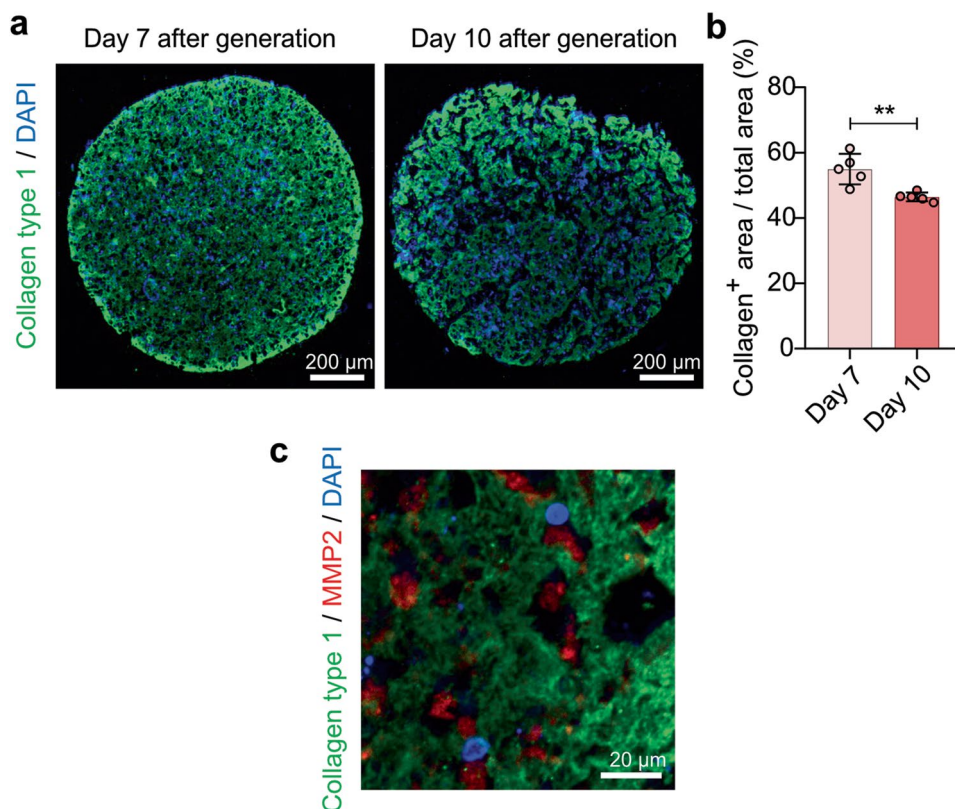
10 or 50 ng/mL TGF- β ($n = 5$ biological replicates examined in one experiment). Images were taken from day 0 to day 15 after fibrosis induction. Line and error bars represent mean \pm s.d.



Extended Data Fig. 3 | Location of MGV microinjected to lung organoids. Stacked fluorescent image of a lung organoid microinjected with Alexa Fluor 488-conjugated MGVs 19 days after microinjection. F-actin was used for cytoskeleton staining, and DAPI was used for staining nuclei ($n = 1$ biological replicates in two experiments).

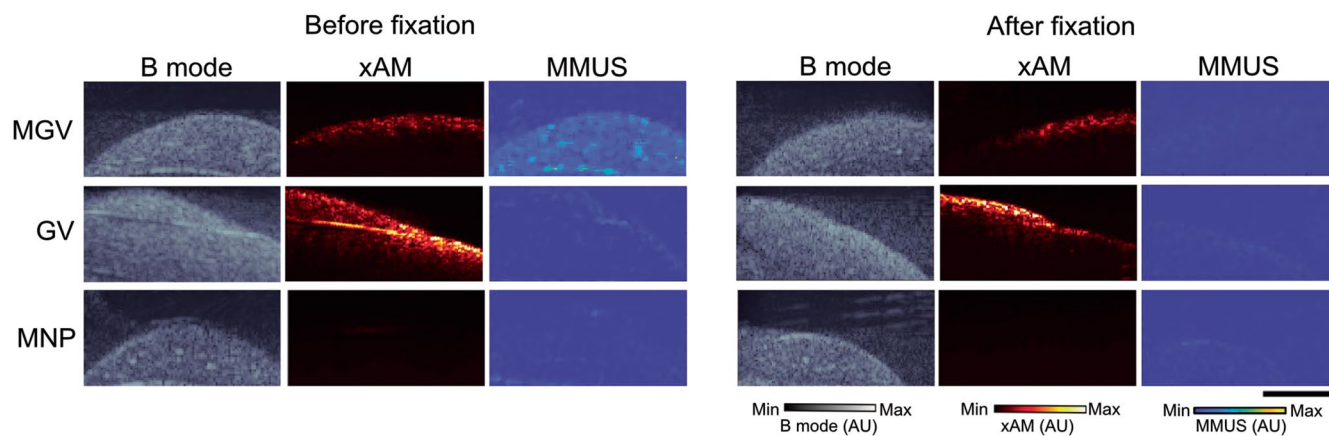


Extended Data Fig. 4 | The comparison of protein expression between lung normal organoids and lung fibrosis organoids. Fluorescent images of MGV-microinjected lung organoids stained with EMT markers (VIM and SMA) and lung epithelial cell markers (α -tubulin, MUC5AC, and P63) 16 days after fibrosis induction by treatment with 50 ng/mL TGF- β . DAPI was used for staining nuclei ($n = 1$ biological replicated in on experiments).



Extended Data Fig. 5 | ECM remodeling in liver organoids. (a) Fluorescent images of normal liver organoid sections stained with collagen type 1 on days 7 and 10 after organoid generation. DAPI was used for staining nuclei ($n = 3$ biological replicates in two experiments). (b) Bar graph quantifying the collagen⁺ area / total area (%) of liver organoids on days 7 and 10 after organoid generation

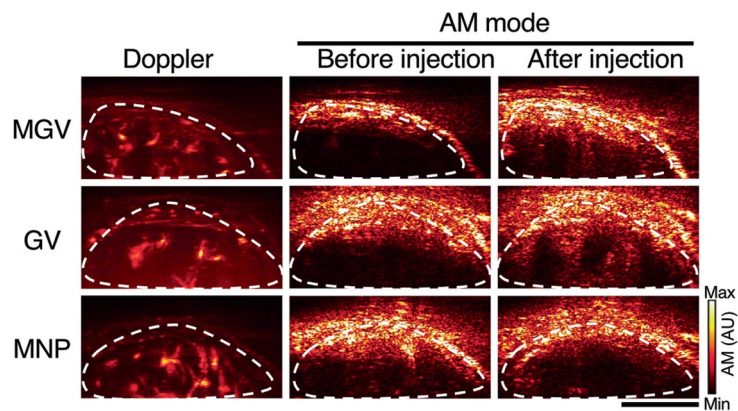
(P value: 0.004374) ($n = 5$ biological replicates). Line and error bars represent mean \pm s.d., and significance was determined using the unpaired two-sided t-test; **: $p < 0.01$. (c) Fluorescent image of normal liver organoid sections stained with collagen type 1 and MMP2 on day 7 after organoid generation. DAPI was used for staining nuclei ($n = 3$ biological replicates in two experiments).



Extended Data Fig. 6 | *Ex vivo* liver imaging before and after fixation.

Three different groups of nanomaterials (MGVs, GVs, or MNPs) were injected intravenously into different cohorts, and after 5 minutes, the liver was extracted to take ultrasound images. Liver was fixed in 10% formalin for 48 h. B-mode images reveal the shape of the liver, xAM images show the GV signal located at

the ultrasound focus, and the Δ images show the MMUS signal ($n = 3$ animals per group). Scale bars, 5 mm. Min and max on color bars for parula (MMUS) and grey (B-mode) colour bar range from 0 to 10000 arbitrary units, and the hot (xAM) colour bar ranges from 0 to 1000000 arbitrary units.



Extended Data Fig. 7 | Tracking GV and MGv delivery using AM and Doppler imaging in the liver. Three different groups of nanomaterials (MGVs, GVs, or MNPs) were injected intravenously into different cohorts, and liver AM and Doppler images were taken after 5 minutes. Doppler images reveal the position

of the liver, AM images show the signal from GVs or MGVs after injection ($n = 3$ animals per group). Scale bars, 5 mm. Min and max on colour bar ranges from 0 to 1000000 arbitrary units.

Reporting Summary

Nature Portfolio wishes to improve the reproducibility of the work that we publish. This form provides structure for consistency and transparency in reporting. For further information on Nature Portfolio policies, see our [Editorial Policies](#) and the [Editorial Policy Checklist](#).

Statistics

For all statistical analyses, confirm that the following items are present in the figure legend, table legend, main text, or Methods section.

n/a Confirmed

- The exact sample size (n) for each experimental group/condition, given as a discrete number and unit of measurement
- A statement on whether measurements were taken from distinct samples or whether the same sample was measured repeatedly
- The statistical test(s) used AND whether they are one- or two-sided
Only common tests should be described solely by name; describe more complex techniques in the Methods section.
- A description of all covariates tested
- A description of any assumptions or corrections, such as tests of normality and adjustment for multiple comparisons
- A full description of the statistical parameters including central tendency (e.g. means) or other basic estimates (e.g. regression coefficient) AND variation (e.g. standard deviation) or associated estimates of uncertainty (e.g. confidence intervals)
- For null hypothesis testing, the test statistic (e.g. F , t , r) with confidence intervals, effect sizes, degrees of freedom and P value noted
Give P values as exact values whenever suitable.
- For Bayesian analysis, information on the choice of priors and Markov chain Monte Carlo settings
- For hierarchical and complex designs, identification of the appropriate level for tests and full reporting of outcomes
- Estimates of effect sizes (e.g. Cohen's d , Pearson's r), indicating how they were calculated

Our web collection on [statistics for biologists](#) contains articles on many of the points above.

Software and code

Policy information about [availability of computer code](#)

Data collection	We used MATLAB (version 2017b or 2020a, Mathworks) custom scripts, with functions provided by the Vantage 4.0.0 or 4.2.0 system (Verasonics), to acquire ultrasound images. All custom code will be available on the Shapiro Lab GitHub (http://github.com/shapiro-lab) upon publication. Software for microscopy were Ocular (version 2.0, Olympus Life Science), EVOS® FL Auto Cell Imaging System (software v.16) and Zen (version 3.0, Zeiss). Software for material characterizations were collected by commercial softwares (e.g., TEM, DigitalMicrograph 3.22.1461.0; VSM, Lake Shore VSM software 4.9.0; ICP-OES, Qtegra 2.6.2270.44; DLS, Zetasizer Software 7.12). For whole liver morphology iPhone 11pro was used. Rheometer software RheoCompass™ (version V1.24.549, Anton Paar) was used. Software for microplate reader is Sparkcontrol (version 3.1 SP1, Tecan). Fiber optic hydrophone version is 1.2.0.27 (Precision Acoustics Ltd).
Data analysis	We used MATLAB (2019a or 2022a, Mathworks) and Prism (version 9, Graphpad) for data and image analysis and plotting. For microscopic imaging analysis Zen (version 3.0, Zeiss), ImageJ (version 1.51j8, NIH) and OlyVIA (version 2.9, Olympus Life Science) was used. For material characterization analysis commercial softwares were used (e.g., TEM, DigitalMicrograph 3.22.1461.0; VSM, Lake Shore VSM Software 4.9.0). Illustrations were made in Affinity Designer (version 1.10.0, Serif Europe).

For manuscripts utilizing custom algorithms or software that are central to the research but not yet described in published literature, software must be made available to editors and reviewers. We strongly encourage code deposition in a community repository (e.g. GitHub). See the Nature Portfolio [guidelines for submitting code & software](#) for further information.

Data

Policy information about [availability of data](#)

All manuscripts must include a [data availability statement](#). This statement should provide the following information, where applicable:

- Accession codes, unique identifiers, or web links for publicly available datasets
- A description of any restrictions on data availability
- For clinical datasets or third party data, please ensure that the statement adheres to our [policy](#)

The data presented in this study are available in the Source data. Additional information and requests for resources and reagents that support the findings of this study are available from the corresponding author upon reasonable request. Source data are provided with this paper.

Human research participants

Policy information about [studies involving human research participants and Sex and Gender in Research](#).

Reporting on sex and gender	To produce lung organoids, fragmented lung tissues were obtained from one male and two female patients. This study was not related to sex and gender and sex-specific analyses were not performed.
Population characteristics	Fragmented human lung tissues from anonymous patients who aged 19 to 80 (male or female) were obtained.
Recruitment	Tissue fragments were collected from patients undergoing lung surgery after acquiring their informed consents. There was no pre-selection on the patients and tissue fragments for lung organoid generation.
Ethics oversight	The use of human lung tissues for lung organoid generation was approved by the Institutional Review Board (IRB) of Severance Hospital (IRB No: 4-2021-1555).

Note that full information on the approval of the study protocol must also be provided in the manuscript.

Field-specific reporting

Please select the one below that is the best fit for your research. If you are not sure, read the appropriate sections before making your selection.

Life sciences Behavioural & social sciences Ecological, evolutionary & environmental sciences

For a reference copy of the document with all sections, see [nature.com/documents/nr-reporting-summary-flat.pdf](https://www.nature.com/documents/nr-reporting-summary-flat.pdf)

Life sciences study design

All studies must disclose on these points even when the disclosure is negative.

Sample size	The numbers of biological and technical replicates were chosen based on preliminary experiments, so as to provide sufficient power for statistical comparison.
Data exclusions	No data were excluded from this study.
Replication	Replicates are reported in the figure legends.
Randomization	Standardized cell culture conditions and samples used in each set of experiments were equal to minimize variation across samples, except the experimental condition being tested. Cultured lung and liver organoids were randomly assigned for each group when they reached the each specified time point. Animals were randomly distributed into cages and ear-punched by animal care staff. Cages of animals were randomly chosen for the experimental groups versus control conditions. In all other experiments, samples were allocated randomly and performed with appropriate control.
Blinding	Blinding was not applicable to our study because our experiments did not involve human participants and was not possible since the main researcher was responsible for both data acquisition and analysis. All data collection, processing, and analysis methods were quantitative and identical across experimental groups.

Reporting for specific materials, systems and methods

We require information from authors about some types of materials, experimental systems and methods used in many studies. Here, indicate whether each material, system or method listed is relevant to your study. If you are not sure if a list item applies to your research, read the appropriate section before selecting a response.

Materials & experimental systems

n/a	Involved in the study
<input type="checkbox"/>	<input checked="" type="checkbox"/> Antibodies
<input type="checkbox"/>	<input checked="" type="checkbox"/> Eukaryotic cell lines
<input checked="" type="checkbox"/>	<input type="checkbox"/> Palaeontology and archaeology
<input type="checkbox"/>	<input checked="" type="checkbox"/> Animals and other organisms
<input checked="" type="checkbox"/>	<input type="checkbox"/> Clinical data
<input checked="" type="checkbox"/>	<input type="checkbox"/> Dual use research of concern

Methods

n/a	Involved in the study
<input checked="" type="checkbox"/>	<input type="checkbox"/> ChIP-seq
<input checked="" type="checkbox"/>	<input type="checkbox"/> Flow cytometry
<input checked="" type="checkbox"/>	<input type="checkbox"/> MRI-based neuroimaging

Antibodies

Antibodies used

The following primary antibodies were used:

Mouse monoclonal (B4) anti-smooth muscle actin (SMA, #sc-53142, 1:50, Santa Cruz Biotechnology)
 Mouse monoclonal (LN-6) anti-vimentin (VIM, #MAB1681, 1:50, Sigma-Aldrich)
 Rabbit monoclonal (EPR5701) anti-P63 (#ab124762, 1:200, Abcam)
 Mouse monoclonal (45M1) anti-MUC5AC (#ab3649, 1:200, Abcam)
 Mouse monoclonal (6-11B-1) anti-acetylated α -tubulin (#sc-23950, 1:50, Santa Cruz Biotechnology)
 Mouse monoclonal (C3) anti-AFP (#sc-8399, 1:50, Santa Cruz Biotechnology)
 Rabbit polyclonal anti-albumin (ALB, #A3293, 1:200, Sigma-Aldrich)
 Rabbit monoclonal (28E1) anti-PDGF receptor β (PDGFRB, #3169, 1:100, Cell Signaling)
 Mouse monoclonal (GA5) anti-glial fibrillary acidic protein (GFAP, #MAB3402, 1:200, Sigma-Aldrich)
 Rabbit polyclonal anti-collagen type 1 (#234167, 1:50, Sigma-Aldrich)
 Mouse monoclonal (8B4) anti-MMP2 (#sc-13595, 1:50, Santa Cruz Biotechnology)
 Goat Anti-Mouse IgG monoclonal, Mouse anti-IgG/HRP conjugate polyclonal(#501240, Cayman chemical)
 Mouse anti-IgM monoclonal, HRP-conjugated anti-mouse Ig(H+L) polyclonal (#88-50470-22, Thermo Fisher Scientific)

The following secondary antibodies were used:

Alexa-Fluor 488-conjugated anti-mouse IgG (#A11001, 1:200, Thermo Fisher Scientific)
 Alexa-Fluor 488-conjugated anti-rabbit IgG (#A11008, 1:200, Thermo Fisher Scientific)
 Alexa-Fluor 594-conjugated anti-mouse IgG (#A11005, 1:200, Thermo Fisher Scientific)
 Alexa-Fluor 594-conjugated anti-rabbit IgG (#A11012, 1:200, Thermo Fisher Scientific)

Validation

All antibodies listed above are commercially available and have been verified by many references provided on the website of the companies that sell antibodies (links below).

Mouse monoclonal (B4) anti-smooth muscle actin (SMA, #sc-53142, 1:50, Santa Cruz Biotechnology)
 Validation Refs. from the manufacturer's datasheet: <https://datasheets.scbt.com/sc-53142.pdf>

Mouse monoclonal (LN-6) anti-vimentin (VIM, #MAB1681, 1:50, Sigma-Aldrich)
 Validation Refs. from the manufacturer's datasheet: <https://www.sigmaaldrich.com/product/mm/mab1681>

Rabbit monoclonal (EPR5701) anti-P63 (#ab124762, 1:200, Abcam)
 Validation Refs. from the manufacturer's datasheet: <https://www.abcam.com/products/primary-antibodies/p63-antibody-epr5701-ab124762.html>

Mouse monoclonal (45M1) anti-MUC5AC (#ab3649, 1:200, Abcam)
 Validation Refs. from the manufacturer's datasheet: <https://www.abcam.com/products/primary-antibodies/mucin-5ac-antibody-45m1-ab3649.html>

Mouse monoclonal (6-11B-1) anti-acetylated α -tubulin (#sc-23950, 1:50, Santa Cruz Biotechnology)
 Validation Refs. from the manufacturer's datasheet: <https://datasheets.scbt.com/sc-23950.pdf>

Mouse monoclonal (C3) anti-AFP (#sc-8399, 1:50, Santa Cruz Biotechnology)
 Validation Refs. from the manufacturer's datasheet: <https://datasheets.scbt.com/sc-8399.pdf>

Rabbit polyclonal anti-albumin (ALB, #A3293, 1:200, Sigma-Aldrich)
 Validation Refs. from the manufacturer's datasheet: <https://www.sigmaaldrich.com/product/sigma/a3293>

Rabbit monoclonal (28E1) anti-PDGF receptor β (PDGFRB, #3169, 1:100, Cell Signaling)
 Validation Refs. from the manufacturer's datasheet: <https://www.cellsignal.com/products/primary-antibodies/pdgf-receptor-b-28e1-rabbit-mab/3169>

Mouse monoclonal (GA5) anti-glial fibrillary acidic protein (GFAP, #MAB3402, 1:200, Sigma-Aldrich)
 Validation Refs. from the manufacturer's datasheet: <https://www.sigmaaldrich.com/product/mm/mab3402>

Rabbit polyclonal anti-collagen type 1 (#234167, 1:50, Sigma-Aldrich)
 Validation Refs. from the manufacturer's datasheet: <https://www.sigmaaldrich.com/product/mm/234167>

Mouse monoclonal (8B4) anti-MMP2 (#sc-13595, 1:50, Santa Cruz Biotechnology)
 Validation Refs. from the manufacturer's datasheet: <https://datasheets.scbt.com/sc-13595.pdf>

Goat Anti-Mouse IgG monoclonal, HRP-conjugated anti-mouse IgG polyclonal (#501240, 1:10, Cayman chemical)
Validation Refs. from the manufacturer's datasheet: <https://www.caymanchem.com/product/501240>

Mouse anti-IgM monoclonal, HRP-conjugated anti-mouse Ig(H+L) polyclonal (#88-50470-22, 1:250, Thermo Fisher Scientific)
Validation Refs. from the manufacturer's datasheet: <https://www.thermofisher.com/elisa/product/IgM-Mouse-Uncoated-ELISA-Kit-with-Plates/88-50470-22>

Eukaryotic cell lines

Policy information about [cell lines and Sex and Gender in Research](#)

Cell line source(s)	Lung organoids were prepared from human lung tissues harvested with the patients' consent. HEK293T-Rspo1-Fc cells were purchased from Calvin Kuo's Laboratory at Stanford University. A human induced pluripotent stem cell (hiPSC) line (CHO) was non-commercial and provided by the Yonsei University School of Medicine. Hepatic endodermal cells and hepatic stellate cells were differentiated from hiPSCs. Human umbilical vein endothelial cells (HUVECs) and human mesenchymal stem cells (hMSCs) were purchased from Lonza. HEK293T cells were ordered from American Type Culture Collection (ATCC).
Authentication	Lung organoids were authenticated with immunostaining of airway markers (P63, MUC5AC, α -tubulin). HEK293T-Rspo1-Fc cells were not authenticated after purchase. hiPSCs were authenticated with immunostaining of pluripotency markers (OCT4, TRA-1-60, SOX2) and alkaline phosphatase staining. HUVECs and hMSCs were authenticated by Lonza before delivery and not authenticated subsequently. HEK293T cells were authenticated by ATCC before delivery using short tandem repeat (STR) profiling.
Mycoplasma contamination	hiPSCs were regularly checked and negative for mycoplasma contamination. HUVECs and hMSCs negative for mycoplasma contamination were purchased and not authenticated subsequently. HEK293T-Rspo1-Fc cells were not authenticated after purchase. HEK293T cells were certified not contaminated by ATCC and not tested from mycoplasma contamination subsequently.
Commonly misidentified lines (See ICLAC register)	No misidentified cell lines were used in this study.

Animals and other research organisms

Policy information about [studies involving animals; ARRIVE guidelines](#) recommended for reporting animal research, and [Sex and Gender in Research](#)

Laboratory animals	Male C57 mice aged 4-8 weeks and Male Balb/C mice aged 4 weeks were used for in vivo experiments. Animal housing room temperatures are monitored at all times and maintained between 71 and 75 degrees F for most species according to their physiological needs. Humidity is maintained between 30-70%. Light intensity and light cycle timing are carefully regulated and monitored in Caltech laboratory animal facilities. Automated light timers ensure a consistent light-dark cycle with 13 hours on and 11 hours off.
Wild animals	This study did not involve wild animals.
Reporting on sex	This study did not involve sex specificity in the study design.
Field-collected samples	This study did not involve samples collected from the field.
Ethics oversight	Institutional Animal Care and Use Committee (IACUC) of the California Institute of Technology (Caltech) for animal experiments.

Note that full information on the approval of the study protocol must also be provided in the manuscript.